

## Monitoring transitions between antiferromagnetic states of individual molecules

Claire Besson,<sup>a,b</sup> Philipp Stegmann,<sup>c,d</sup> Michael Schnee,<sup>b</sup> Zeila Zanolli,<sup>e,f</sup> Simona Achilli,<sup>e,g</sup> Nils Wittmeier,<sup>e</sup> Asmus Vierck,<sup>h</sup> Robert Frielinghaus,<sup>b</sup> Paul Kögerler,<sup>b,i</sup> Janina Maultzsch,<sup>h,j</sup> Pablo Ordejón,<sup>e</sup> Claus M. Schneider,<sup>b</sup> Alfred Hucht,<sup>c</sup> Jürgen König,<sup>c</sup> Carola Meyer<sup>k,b\*</sup>

- a. Department of Chemistry, The George Washington University, Washington DC, USA
- b. Peter Grünberg Institut (PGI-6), Forschungszentrum Jülich, 52425 Jülich, Germany and Jülich Aachen Research Alliance (JARA)–Fundamentals of Future Information Technology, 52425 Jülich, Germany
- c. Theoretische Physik, Universität Duisburg-Essen and CENIDE, 47048 Duisburg, Germany
- d. Current affiliation: Department of Chemistry, Massachusetts Institute of Technology, Cambridge, Massachusetts 02139, USA
- e. Chemistry Department and ETSF, Debye Institute for Nanomaterials Science, Condensed Matter and Interfaces, Utrecht University, PO Box 80.000, 3508 TA Utrecht, The Netherlands
- f. Catalan Institute of Nanoscience and Nanotechnology (ICN2), CSIC and BIST, Campus UAB, Bellaterra, 08193 Barcelona, Spain
- g. Dipartimento di Fisica "Aldo Pontremoli", Università degli Studi di Milano, Via Celoria 16, Milan, Italy
- h. Institut für Festkörperphysik, Technische Universität Berlin, Hardenbergstrasse 36, 10623 Berlin, Germany
- i. Institute of Inorganic Chemistry, RWTH Aachen University, 52074 Aachen, Germany
- j. Department of Physics, Friedrich-Alexander University Erlangen-Nürnberg, Staudtstrasse 7, 91058 Erlangen, Germany
- k. Fachbereich Physik, Universität Osnabrück, D-49069 Osnabrück, Germany

## Abstract

Spin-electronic devices are poised to become part of mainstream microelectronic technology. Downsizing them, however, faces the intrinsic difficulty that as ferromagnets become smaller, it becomes more difficult to stabilize their magnetic moment. Antiferromagnets are much more stable, and thus research on antiferromagnetic spintronics has developed into a fast-growing field. Here, we provide proof of concept data that allows us to expand the area of antiferromagnetic spintronics to the hitherto elusive level of individual molecules. In contrast to all previous work on molecular spintronics, our detection scheme of the molecule's spin state does not rely on a magnetic moment. Instead, we use the step-like transitions between several distinct current levels caused by transitions between different antiferromagnetic states of an individual molecule grafted onto a carbon nanotube. We find that in the absence of an orbital momentum the antiferromagnetic spin states of the molecules show coherent superposition.

Antiferromagnetic spintronics is emerging as a promising field for technologies ranging from magnetic random access memories to neuromorphic computing and THz information devices, as antiferromagnets (AFMs) do not produce any, and are insensitive towards, magnetic stray fields<sup>1-4</sup>. The lack of a net magnetic moment confers high stability to the antiferromagnetic states but, at the same time, makes it challenging to address and differentiate among them. Therefore, this area has not yet been extended to the level of individual molecules exhibiting antiferromagnetically coupled magnetic spin centres, while spintronics with e.g. high-spin single molecule magnets (SMMs) are by now well-established<sup>5,6</sup>. In this letter, we showcase how transitions between molecular  $S_{\text{tot}} = 0$  spin states can be monitored via charge transport when the molecules are coupled to a carbon nanotube quantum dot. Transitions between different antiferromagnetic states are accompanied by step-like changes of the current through the quantum dot, resulting in a random telegraph signal (RTS). This method of investigation paves the way to explore the molecular equivalent of AFM spintronics, leading to new molecular spintronic devices characterised by states that do not couple to dipolar fields, and are therefore more robust than those in ferromagnetic systems. Modelling the RTS, we find that such robust states can exhibit a coherent superposition with exceptionally long coherence times.

In the past years significant progress has allowed detecting spin states of individual molecules using scanning tunnelling microscopy<sup>7-17</sup> or molecules in junctions<sup>18-21</sup>. However, in these approaches the electric bias field applied to the molecule will in general influence its charge state, and therefore its magnetic characteristics. To circumvent this issue, it has been proposed to detect the spin state of an SMM by grafting it to a non-magnetic one-dimensional conductor (such as a carbon nanotube, CNT) and measuring the magnetic state of the so-obtained hybrid system<sup>22</sup>. CNTs have been used successfully to read out states of SMMs by measuring the magnetoresistance effect<sup>23</sup>, detecting phonon-spin interaction<sup>24</sup> and spin interactions within an individual SMM<sup>25</sup>. All these experiments depend on the detection of a local magnetic moment. Therefore, they cannot be employed for single-molecule antiferromagnets that have no resulting magnetic moment. We show here that transitions between different  $S_{\text{tot}} = 0$  eigenstates lead to a random telegraph signal in a CNT quantum dot, which can thus be used to map such states.

To fabricate a system that expresses different molecular  $S_{\text{tot}} = 0$  states, we use charge-neutral molecular  $[\text{M}_4\text{L}_2(\text{OAc})_4]$  complexes<sup>26,27</sup> ( $\text{H}_2\text{L} = 2,6\text{-bis-(1-(2-hydroxyphenyl)iminoethyl)pyridine}$ ;  $\text{HOAc} = \text{acetic acid}$ ;  $\text{M} = \text{Mn}^{\text{II}}$  or  $\text{Co}^{\text{II}}$ ). Those complexes (hereafter denoted as  $\{\text{Mn}_4\}$  and  $\{\text{Co}_4\}$ ) display a quasi-tetrahedral core of divalent metal ions interlinked by ligands (inset Fig. 1). Exchange coupling between the metal ions is mediated mainly by four oxygen atoms of the ligands, each bridging between three metal centres into a nearly cubic  $\text{M}_4\text{O}_4$  core, which can be thought of as two pairs of antiferromagnetically interacting ions. Each of the four ions resides in an approximately octahedral or trigonal bipyramidal ligand field with a spin  $S = \frac{5}{2}$  ( $S = \frac{3}{2}$ ) for  $\text{Mn}^{\text{II}}$  ( $\text{Co}^{\text{II}}$ ).

The total spin of the complex  $\vec{S}_{\text{tot}} := \sum_i \vec{S}_i$  is characterized by the spin quantum number  $S_{\text{tot}}$  and the magnetic quantum number  $S_{\text{tot}}^z$ . To form a complete set of quantum numbers, we (arbitrarily) group the four spins into two pairs and include the spin quantum numbers  $S_{12}$ ,  $S_{34}$  of the two spin pairs  $\vec{S}_{ij} := \vec{S}_i + \vec{S}_j$  so that  $\vec{S}_{\text{tot}} = \vec{S}_{12} + \vec{S}_{34}$  (Fig. S1 and Supplementary section SI-1 Discussion of spin states). The ground state is antiferromagnetic with  $S_{\text{tot}} = S_{\text{tot}}^z = 0$  as supported by magnetisation measurements.<sup>27,28</sup>

Density Functional Theory (DFT) calculations of the isolated complexes<sup>27</sup> also yield an  $S_{\text{tot}}^z = 0$  ground state, confirming the overall antiferromagnetic nature of the intramolecular magnetic interactions in the simpler one-electron approximation. If the exchange couplings between all ions were uniform, the  $S_{\text{tot}} = S_{\text{tot}}^z = 0$  ground state would exhibit a six-fold (four-fold) degeneracy for  $\{\text{Mn}_4\}$  ( $\{\text{Co}_4\}$ ). The four degenerate states for  $\{\text{Co}_4\}$  would correspond to  $|S_{\text{tot}}, S_{\text{tot}}^z, S_{12}, S_{34}\rangle = |0, 0, 0, 0\rangle, |0, 0, 1, 1\rangle, |0, 0, 2, 2\rangle, |0, 0, 3, 3\rangle$ , to which the  $|0, 0, 4, 4\rangle$  and  $|0, 0, 5, 5\rangle$  states would be added for  $\{\text{Mn}_4\}$  (Supplementary section SI-1). This degeneracy is lost in the molecular complexes due to the presence of the ligands that render the magnetic atoms inequivalent.

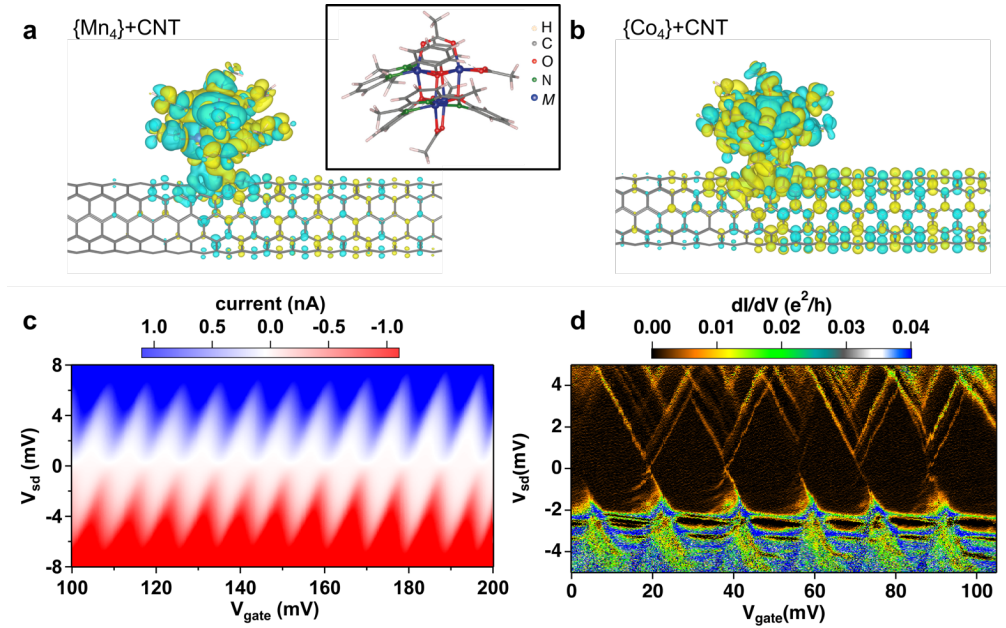


**Figure 1** Calculated spin density and experimental quantum transport properties of the devices. Spin density ( $\rho_{\uparrow} - \rho_{\downarrow}$ ) on the **a**, CNT- $\{\text{Mn}_4\}$  **b**, CNT- $\{\text{Co}_4\}$  hybrid system computed from first principles in an open-system setup<sup>29-31</sup>. Light blue and yellow indicate positive and negative values of the isosurfaces normalised to the maximum spin density. The inset depicts the general structure of the molecules. **c**, Stability diagram of the quantum dot formed on the  $\{\text{Mn}_4\}$ -functionalised CNT, measured at a temperature of 4 K ( $B = 0$  T), exhibiting a very clean and regular pattern of Coulomb diamonds with a quantum dot size comparable to the distance between the electrodes<sup>32</sup>. **d**, Coulomb diamonds of a CNT quantum dot functionalised with  $\{\text{Co}_4\}$  complexes ( $B = 0$  T), revealing an even-odd pattern with  $\Delta E \sim 0.7$  meV that fits very well to the distance of 700 nm between the contacts that form the confining potential barriers<sup>33</sup>. The width of the current steps as well as that of the Coulomb peaks yield an electron temperature of 600 mK.

The complexes retain their antiferromagnetic nature when grafted covalently to the CNT (Fig. 1a,b) by a metathesis reaction between an acetate ligand of the complex and a carboxylic acid group generated by oxidation of the tube<sup>28</sup>. This chemical functionalisation induces a further reduction of the symmetry, enabling transitions between ground and

excited singlet states (an example for an excited state is given in Supplementary section SI-1). Our DFT calculations confirm the overall antiferromagnetic nature of the ground state of the grafted complexes and demonstrate that the interaction between each individual molecule and the CNT is similar for  $\{\text{Co}_4\}$  and  $\{\text{Mn}_4\}$ : the electronic properties of the nanotube around the Fermi energy are slightly perturbed by the molecule, and the total spin polarization of the hybrid system is larger for  $\{\text{Co}_4\}$ -CNT than for  $\{\text{Mn}_4\}$ -CNT (Supplementary section SI-2). We used an open-system approach<sup>29-31</sup> to demonstrate that the spin polarisation induced on the nanotube at the grafting site is long-ranged (Fig. 1a,b) with a decay determined by the CNT electronic structure (SI-2).

A key difference between the two molecules is the value of the orbital momentum: finite in  $\text{Co}^{\text{II}}$  in agreement with the  $3d^7$  atomic configuration, almost negligible in  $\text{Mn}^{\text{II}}$  due to the half filling of the 3d shell. By including spin orbit coupling in the DFT calculations we verified that the orbital momentum of cobalt is practically fully quenched for the two trigonal bipyramidal metal centers, while a significant orbital moment (0.18 and 0.25  $\mu_B$ , open-system approach) is found for the two octahedrally coordinated atoms (Supplementary section SI-2).

Individual CNTs functionalised with either  $\{\text{Mn}_4\}$  or  $\{\text{Co}_4\}$  complexes are contacted in a field-effect transistor structure with highly doped silicon serving as back gate. The number of complexes within a device is derived from our previous experimental evaluation<sup>28</sup> of the functionalisation density – approximately one complex every 10 nm. Raman spectroscopy of the device with  $\{\text{Mn}_4\}$  complexes is used to identify the chirality of the CNT based on analysis of the G-mode<sup>34</sup>. It shows a metallic tube according to the strong broadening of the  $G^{(-)}$ -mode<sup>34</sup> (Fig. S6); resonance behaviour and position of  $G^{(-)}$  and of the TO+ZA combination mode<sup>35</sup> allow for an assignment to the family  $2n + m = 30$  (where  $(n, m)$  is the CNT chiral index) and the absence of the TO peak suggests a zigzag (15,0) CNT, where the TO mode is Raman-inactive. Accordingly, no transport gap is found in the electrical measurements. This is consistent with our first-principles prediction of a metallic character for the hybrid CNT- $\{\text{M}_4\}$  systems (Fig. S3 and Supplementary section SI-2). The stability diagrams of the quantum dots bearing about 50  $\{\text{Mn}_4\}$  complexes or 70  $\{\text{Co}_4\}$  complexes exhibit regular Coulomb diamonds (Fig. 1c,d) with a quantum dot size comparable to the distance between the electrodes. Thus, the covalent grafting of complexes to the CNT does not cause strong localisation within the devices.

Figure 2a shows a short section of the current trace taken at 30 mK at the edge of the Coulomb diamond of a  $\{\text{Mn}_4\}$  functionalized CNT device. The probability density function (PDF) corresponding to the entire trace (one hour length), reported in Figure 2a, exhibits a quasi-exponential decay instead of a single Gaussian peak. A similar signal is measured at an equivalent position of a CNT quantum dot functionalised with  $\{\text{Co}_4\}$  complexes (Fig. 2c). While it does clearly not resemble a single Gaussian peak, the asymmetry of the PDF is much less prominent compared to the  $\{\text{Mn}_4\}$  device and the signal decays much faster.

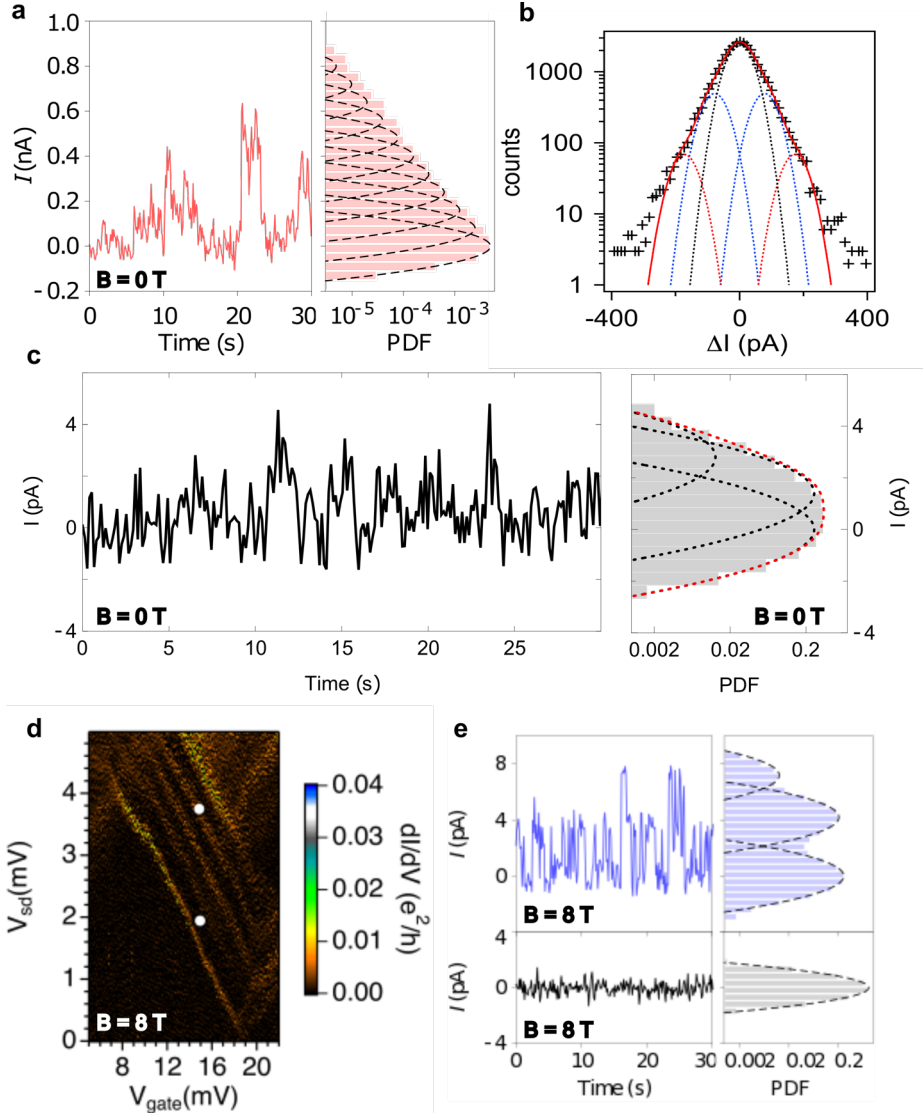


**Figure 2 Random telegraph signals of  $\{M_4\}$  functionalised CNTs.** **a**, Short section of the time trace of the current at the edge of a Coulomb diamond of the  $\{Mn_4\}$ -functionalised CNT quantum dot and PDF of the entire one hour signal displayed with 11 Gaussian peaks indicating the current levels (we omit the 3 highest levels for better visibility). **b**, Histogram of the derivative of the entire signal (note the logarithmic scale) fitted with five Gaussian peaks leading to a standard deviation of the original signal  $\sigma_{\text{original}} = \sigma_{\text{deriv}} / \sqrt{2} = 40$  (1) pA respectively. **c**, Short section of the current trace at the edge of a Coulomb diamond of the  $\{Co_4\}$ -functionalised CNT quantum dot and corresponding PDF of the entire signal (1300 s) with three Gaussian peaks fitted at  $B = 0$  T. **d**, Part of the stability diagram of a CNT quantum dot functionalised with approx. 70  $\{Co_4\}$ - complexes at  $B = 8$  T (perpendicular to CNT axis). White dots indicate the positions where the current traces shown in e were measured (gate and bias voltage of the lower point the same as in c). **e**, Parts of the time traces of the current taken at the indicated positions in d (top, in blue, for  $V_{\text{sd}} = 3.9$  mV, bottom, in black, for  $V_{\text{sd}} = 2.0$  mV) with the respective PDF of the entire original current traces after background correction on the right. Discrete current levels are indicated by dashed lines.

Studying the derivative of the original signal of the  $\{\text{Mn}_4\}$ -device (see Fig. 2b) with respect to time, we extract the largest possible value between two current levels to be  $\Delta I \sim 80$  pA and the standard deviation of  $\sigma_{\text{deriv}} = \sqrt{2} \sigma_{\text{original}} = 56.4 (1.3)$  pA, with the standard deviation of the original signal  $\sigma_{\text{original}}$  (see Supplementary section SI-4 for an extended discussion). The PDF of the original signal can thus be fitted by equidistant Gaussian peaks with  $\text{FWHM} = 2 \sqrt{2 \ln(2)} \sigma_{\text{original}} = 94$  pA. This results in at least 14 equidistant current levels. Each level is directly related to an energy that can be evaluated from the current-voltage curve taken at this gate voltage. We find a maximum spacing of  $\Delta \varepsilon \sim 27 \mu\text{eV}$ . (The level spacing  $\Delta \varepsilon$  might be in fact smaller, but this is beyond our resolution. This would lead to more levels, but in fact leave the main results discussed below qualitatively unchanged.)

The larger spin polarization and orbital momentum in the  $\{\text{Co}_4\}$ -CNT, predicted by DFT, will result in a stronger response to an external magnetic field of the former hybrid system. Figure 2d presents a part of the stability diagram of the  $\{\text{Co}_4\}$  device taken at  $B = 8$  T. Exemplary current traces measured at two positions (white dots) are shown in Figure 2e. The background noise in the Coulomb blockade and on the plateaus of the Coulomb staircase shows a Gaussian distribution as expected (Fig. 2e, lower trace). Between two plateaus where the slope of the current change is steepest the current traces exhibit a clear random telegraph signal (Fig. 2e, upper trace).

Indeed, three different current levels with larger energy splitting compared to  $B = 0$  T are clearly identified in the respective PDF. We find that the steps between two adjacent energy levels are equidistant with  $\Delta \varepsilon \sim 0.1$  meV. Fitting three Gaussian peaks to the PDF we find similar amplitudes for the signals with and without a magnetic field applied. While the energetic splitting at  $B = 0$  T is of similar size compared to the signal of the  $\{\text{Mn}_4\}$  functionalized sample, it is obvious that it decays much faster, prohibiting a meaningful statistical analysis.

We interpret the current fluctuations in the following way: from time to time an electron tunnelling through the quantum dot provides the energy to excite the combined system of CNT quantum-dot and all attached molecules. The excitation energy  $\Delta \varepsilon$  is that of a single  $\{\text{M}_4\}$  complex (Fig. 3a). The excited state is thereafter probed by many following electrons that experience a state-dependent tunnelling rate, contributing a characteristic total current. Multiple molecules can be present in an excited state at any given time (with energy  $\Delta \varepsilon$  each), leading to the multi-level PDF of the current. For relaxation, the  $\{\text{M}_4\}$  complexes dissipate their energy to the quantum-dot electrons.

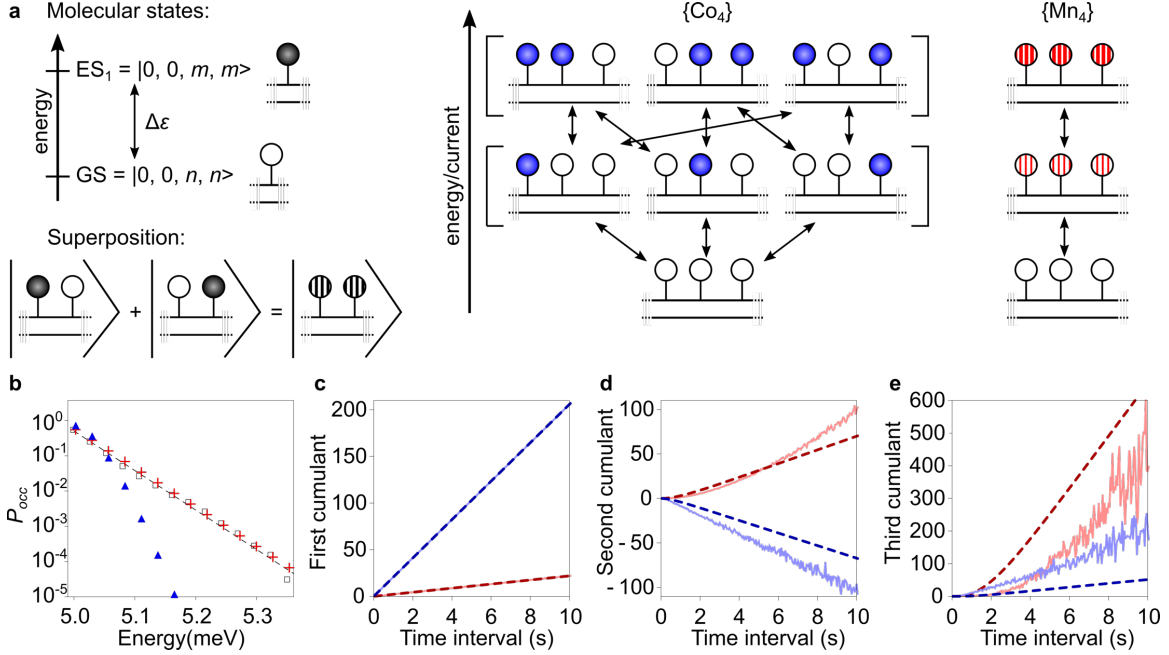


**Figure 3 Analysis of the random telegraph signals.** **a**, Sketch of the different  $|S_{tot}, S_{tot}^z, S_{12}, S_{34}\rangle$  states of the system (with  $n, m = 0, 1, 2, 3, 4, 5$   $_{\{Mn_4\}}$ ,  $n \neq m$ ). Molecules can be in their ground state (open circles), the first excited state (full circles) or a superposition thereof (striped circles). The higher the current level, the more molecules are in an excited state. Here, only three of the attached molecules are shown with the possible transitions. In case of  $\{Co_4\}$ , the different transitions are independent. For  $\{Mn_4\}$ , the states exist in a superposition and thus, the transitions are correlated. **b**, Occupation probability of the different levels found in the  $\{Mn_4\}$ -device on a logarithmic scale for the original data (black squares), and for models assuming 50 independent two-level fluctuators (blue triangles), and 50 coherently coupled two-level fluctuators (red crosses). The dashed line is a fit of the data to an exponential distribution. **c**, First factorial cumulant ( $C_{F,1}$ ) as extracted from the measurements on the CNT quantum dots functionalised with  $\{Mn_4\}$  (red)  $\{Co_4\}$  (blue) complexes. Fits (dashed lines) yield the transition rates used for modelling in **d**, the second ( $C_{F,2}$ ), and in **e**, the third ( $C_{F,3}$ ) factorial cumulant. The solid line in **c**, **d**, **e** are the respective cumulants extracted directly from the digitised measurement signal of the two devices ( $\{Mn_4\}$ : red,  $\{Co_4\}$ : blue). The positive second cumulant in **b** is related to a super-Poissonian Fano factor by  $F = (C_{F,2}/C_{F,1}) + 1$ . All lines of the  $\{Co_4\}$  sample are multiplied by a factor of 20 for better visibility.

The energy difference between the excited states sampled by the current in  $\{\text{Mn}_4\}$  (0.027 meV), and in  $\{\text{Co}_4\}$  (0.1 meV) is orders of magnitude smaller than other processes known to cause RTS in CNT devices.<sup>36-38</sup> Thus, we conclude that the excitation of the quantum dots is due to excitation of non-degenerate molecular  $S_{\text{tot}} = 0$  eigenstates. Note, that these transitions do not involve spin flips as those would require comparably large energies (see Supplementary section SI-2). Instead, different linear superpositions of spin pairs yielding  $S_{\text{tot}}^z = 0$  differ in energy because of non-equivalent exchange interactions between them (Fig. 3a and Supplementary information SI-1).

A statistical analysis of the RTSs, based on factorial cumulants<sup>39</sup>  $C_{F,m}(t)$  with  $m=1,2,3,\dots$ , reveals a fundamental difference in the excitation of the  $\{\text{Co}_4\}/\{\text{Mn}_4\}$  ensembles (for a detailed discussion see Supplementary section SI-5). For the  $\{\text{Co}_4\}$ -functionalised CNT, we assume *independent* two-level fluctuators that can be excited *individually*; here, the sign of the factorial cumulants should alternate,<sup>39-41</sup>  $C_{F,m}(t) \sim (-1)^{m-1}$ , in line with our experimental data (blue curves in Fig. 3 c-e).

Assuming 70  $\{\text{Co}_4\}$  complexes, we extract from the first factorial cumulant the transition rates. These are used to calculate the second and third factorial cumulant (dashed lines in Fig. 3d and e), resulting in good agreement with the measured data at  $B = 8$  T. For the  $\{\text{Mn}_4\}$ -functionalised CNT (red curves in Fig. 3 c-e), the assumption of independent two-level fluctuators can be ruled out due to the wrong sign of the second cumulant. Instead, we assume 50  $\{\text{Mn}_4\}$  complexes that are *collectively* excited by forming a *coherent* superposition of excitations in *all* molecules. This model (with transition rates determined from fitting the first cumulant) correctly reproduces the second and third cumulant (Fig. 3d and e) as well as the exponential occupation probability distribution of the data (Fig. 3b, Fig. S9b). The occupation probabilities  $P_{\text{occ}}$  of the levels depend on the transition rates between adjacent levels (Fig. S8). This behaviour is incompatible with independent excitations of individual  $\{\text{Mn}_4\}$  complexes as this would yield a binomial distribution of  $P_{\text{occ}}$ . Assuming a thermally activated process, we find an activation temperature of 450 mK, in good agreement with the electron temperature of 600 mK.

Since a model of independent three-level fluctuators also fails to reproduce the data (Fig. S9b), we conclude that long-lived coherent excitations involving *all*  $\{\text{Mn}_4\}$  complexes are present in our system. The long coherence time in the order of seconds is, indeed, likely if both the ground and the excited state of the  $\{\text{Mn}_4\}$  complexes do not carry a magnetic moment that could couple to any dipolar (magnetic or electric) field.

In the  $\{\text{Co}_4\}$  device, on the other hand, the  $\text{Co}^{\text{II}}$  ions in their octahedral ligand fields possess a considerable orbital moment. Though the applied magnetic field is not large enough to change the antiferromagnetic nature of the ground state (Supplementary section SI-2), the residual orbital moment couples to fluctuations of dipolar fields leading to fast decoherence due to spin-orbit coupling.<sup>42,43</sup>

In conclusion, we monitor individual transitions between non-degenerate  $S_{\text{tot}} = 0$  states in small ensembles of molecular antiferromagnets (AFMs) by measuring the random telegraph signal of carbon nanotube quantum dots. Analysis of the RTSs statistics finds that while complexes based on magnetic  $\text{Co}^{\text{II}}$  ions switch independently, their congeners based on  $\text{Mn}^{\text{II}}$  ions exhibit a long-lived *coherent superposition* between the states of all molecules attached to the quantum dot. This leads to a fundamentally new perspective on information processing with magnetic molecules. Molecular antiferromagnetic coupling between individual molecules in the order of 100 K is well known.<sup>44</sup> Hence, it appears



feasible to design antiferromagnetic molecules with non-degenerate  $S_{\text{tot}} = 0$  eigenstates that exhibit similar strong coupling, causing a larger separation in energy than the molecules presented here, enough to prevent switching between states caused by temperature. Instead, by inducing dipolar moments, Raman transitions could be driven to change states deliberately. Alternatively, similar control could be reached using tunable exchange interactions  $J$  to modify the energetic order of  $S_{\text{tot}} = 0$  states. The difference in behaviour of both molecular systems investigated here reveals the large impact of even small residual orbital moments on the spin coherence in molecular AFMs. In the complete absence of such moments strikingly long coherence times in the order of seconds can be achieved. While the molecules do not couple to external dipolar fields, their coupling to each other is mediated by the conduction electrons of the CNT. While the molecules do not couple to external dipolar fields, their coupling to each other is mediated by the conduction electrons of the CNT. This offers means of controlling the device: using ferromagnetic contacts, spin polarised electrons can be injected into the CNT<sup>45</sup> and the spin polarization of the conduction electrons can be controlled using a gate.<sup>46</sup> The exploitation of the coherence between *antiferromagnetic* states opens a novel direction in molecular quantum spintronics that has yet to be explored.

## Methods

### Atomistic simulations

First principles simulations of the  $\{M_4\}$ -CNT systems (with  $M = \text{Mn, Co}$ ) were performed using the SIESTA<sup>47</sup> implementation of Density Functional Theory (DFT), within the Local Spin Density Approximation (LSDA). The  $\{M_4\}$  complex are bound via a  $-\text{CO}_2^-$  group to the dangling C of a mono-vacancy site on the external wall of a metallic armchair (5, 5) nanotube. The choice of a metallic nanotube ensures that electron conduction is allowed around the Fermi energy. We have shown that the oxygenated vacancy is especially favourable for functionalisation of CNTs with  $\text{CO}_2$ <sup>29</sup> or magnetic nanoparticles<sup>30</sup>. We performed simulations of a single molecule grafted to an infinite tube using the *open-system* set up of Ref. [31], combining the non-equilibrium Green's function formalism with a DFT Hamiltonian as implemented in TransSIESTA.<sup>48</sup> This is necessary to avoid artefacts resulting from the long range character of the indirect exchange coupling between magnetic clusters mediated by the conduction electrons of the carbon nanotube.<sup>49</sup> The simulation set-up was composed of a central region of 35 CNT-rings (86 Å long) contacted by two semi-infinite (5,5)-CNTs on each side. Further technical details are provided in Supplementary section SI-1.

### Synthesis of the $\{M_4\}$ complexes and chemical functionalisation of the CNTs

$[\text{Mn}_4\text{L}_2(\text{OAc})_4]$  and  $[\text{Mn}_4\text{L}_2(\text{OAc})_4]$  ( $\text{H}_2\text{L} = 2,6\text{-bis-(1-(2-hydroxyphenyl)iminoethyl)pyridine}$ ,  $\{\text{Mn}_4\}$  and  $\{\text{Co}_4\}$ ) were synthesised according to the literature.<sup>26,27</sup> Functionalisation of the carbon nanotube was achieved by introducing the oxidised nanotube device in a solution of the complex of choice (ca. 20 mL of 10 mM solution in  $\text{CH}_3\text{CN}$  for  $\{\text{Mn}_4\}$ , same conditions in  $\text{CH}_2\text{Cl}_2$  for  $\{\text{Co}_4\}$ ) for a week, followed by rinsing in fresh solvent (approx. 20 mL) for a week to remove any non-covalently attached complex.

### Device fabrication and electronic measurements

Electronic devices were fabricated as described in Schnee et al.<sup>32</sup> The CNTs for the sample functionalised with  $\{\text{Co}_4\}$  complexes were oxidised before contact fabrication, since we found that this increases significantly the yield of working devices.

All electronic measurements were carried out in a  $^3\text{He}/^4\text{He}$  dilution refrigerator at a base temperature around 100 mK. The bias voltage was supplied symmetrically via digital-to-analogue converters, addressed via an optical fiber in order to decouple it from the mains. The electron temperature was determined from the width of the coulomb-peaks and independently by fitting a Fermi-function to the first current step (ground state tunneling) of the Coulomb-staircase taken from the  $\{\text{Co}_4\}$ -CNT stability diagram. The current of the noise traces was measured by averaging over 20 ms (NPLC 1) using an HP34401A. In total we had four devices that exhibited regular Coulomb diamonds after cool-down. All of them exhibited random telegraph signals. Two of the devices are discussed in this paper.

### Raman spectroscopy

Confocal micro-Raman spectroscopy was performed at room temperature in backscattering geometry with a Horiba Jobin Yvon LabRAM HR800 monochromator. For this, a He-Ne laser emitting at 633 nm was focused through a 100x microscope objective with 0.95 NA, and the power was kept at 0.7 mW (as measured before the objective). With the help of previously acquired SEM images of the device,<sup>32</sup> the sample was oriented such that the nanotube is aligned parallel to the laser polarisation in order to maximise the signal. The target area was mapped with a motorised stage to find the precise nanotube's position through its Raman signal, and the depth-focus was subsequently adjusted on the nanotube for maximal intensity.

The Raman spectra were spectrally calibrated by the emission lines of a neon lamp. The background signal that is caused by Raman scattering with the device's silicon wafer was measured with  $\sim 2 \mu\text{m}$  lateral distance to the nanotube, which allowed for subsequent subtraction from the signal.

### Data analysis

We used the histogram of the derivative of the original data (before background correction) of the  $\{\text{Mn}_4\}$  functionalised device to determine current steps of  $\Delta I \approx 80 \text{ pA}$  with a standard deviation of  $\sigma_{\text{original}} = 40 (1) \text{ pA}$  (see Fig. 2b). To digitise the random telegraph signal, the background of the noise traces was removed using the statistics-sensitive nonlinear iterative peak clipping (SNIP) algorithm implemented in the computer algebra system Wolfram *Mathematica*. The PDFs and cumulants were determined from a current time trace of 1300s (3600s) length for the  $\{\text{Co}_4\}$  functionalised ( $\{\text{Mn}_4\}$  functionalised) device. The models used to simulate the data are elaborated in the supporting information.

If we separate the time trace of the RTS into time intervals of length  $\Delta t$  and count the number of transitions from higher to lower levels (or equivalently from lower to higher levels), we obtain the probability distribution  $P_N(\Delta t)$  that  $N$  transitions have occurred. This probability distribution can be characterised by so-called factorial cumulants, which are derived in the following way. First, one constructs the generating function, given by the  $z$ -transform of the probability distribution.<sup>39-41</sup> Performing the  $m$ -th derivative of the generating function with respect to  $z$  lead to the factorial moment of order  $m$ , which is nothing but the expectation values of  $N(N-1) \dots (N-m+1)$ , i.e.  $\langle N(N-1) \dots (N-m+1) \rangle$ .

$1)\rangle = \partial_z^m M_F(z, \Delta t)|_{z=0}$ . The *factorial cumulant* of order  $m$  is obtained by the corresponding derivative of the logarithm of the generating function,

$$C_{F,m}(\Delta t) = \langle\langle N(N-1) \dots (N-m+1) \rangle\rangle = \partial_z^m \ln M_F(z, \Delta t)|_{z=0}$$

Factorial cumulants are particularly suited to highlight deviations from a Poisson process since for the latter all factorial cumulants of order  $m \geq 2$  vanish.

### Data availability

Crystal structure data of the new  $\{M_4\}$  complexes are available at Cambridge Structural Database, CCDC 1855019 for  $\{Co_4\}$  and CCDC 1855020 for  $\{Zn_4\}$ .

The data that support the findings of this study are available within the paper and the Supporting information. Additional data are available from the corresponding author upon reasonable request.

### Acknowledgements

The authors thank Christopher Nakamoto for helping with carrying out the synthesis and crystallisation of the tetranuclear complexes and Christian Lurz for valuable discussions about the data analysis. We acknowledge financial support by the Deutsche Forschungsgemeinschaft (DFG) under Project-ID 278162697 – SFB 1242 as well as for individual grants numbers MA 4079/10-1, ME 3275/6-1, and ZA 780/3-1. PS acknowledges support from the German National Academy of Sciences Leopoldina (Grant No. LPDS 2019-10). Furthermore, ZZ acknowledges funding by the Ramón y Cajal programme RYC-2016-19344 (MINECO/AEI/FSE, UE), and the Netherlands sectorplan program 2019-2023. ZZ, SA and NW acknowledge computer time from PRACE on Archer (EU grant RI-653838) and on MareNostrum4 at Barcelona Supercomputing Center (BSC), Spain (OptoSpin project id. 2020225411), from JARA-HPC (project JHPC39), and from RES (projects FI-2020-1-0014, FI-2020-1-0018, FI-2020-2-0034) on MareNostrum4. ZZ, SA, NW and PO acknowledge the EC H2020-INFRAEDI-2018-2020 MaX Materials Design at the Exascale CoE (grant No. 824143), FIS2015-64886-C5-3-P, Severo Ochoa Centers of Excellence Program (Grant No. SEV-2017-0706), and Generalitat de Catalunya CERCA programme (2017SGR1506). NW acknowledges funding from the EU-H2020 research and innovation programme under the Marie Skłodowska-Curie programme (Grant No. 754558). This work benefited from the access provided by ICN2 (Barcelona, Spain) within the framework of the NFFA-Europe Transnational Access Activity (grant agreement No 654360, proposal ID 753, submitted by CM). J.M. and A.V. acknowledge funding under ERC grant no. 259286. C.M. acknowledges funding by Niedersächsisches Vorab Akz. 11-76251-14-3/15(ZN3141).

### Author contributions

P.S. and M.S. contributed equally. C.B. and C.M. conceived the idea. C.B. synthesized and characterized the  $\{Mn_4\}$  and the  $\{Co_4\}$  complexes. R.F. fabricated the  $\{Mn_4\}$  device. M.S. fabricated the  $\{Co_4\}$  device and performed all electrical measurements. C.B., M.S., and C.M. analysed the experimental data. P.S. did the statistical analysis and the modelling of the data. A.H. and J.K. contributed to the modelling and the interpretation of the statistical analysis. Z.Z. planned the first-principles calculations. Z.Z., S.A., N.W., and P.O.

performed, discussed, and interpreted the first-principles calculations. Raman measurements were performed by A.V. and J.M. contributed to their interpretation. The manuscript was written by C.M. with contributions from all authors.

#### Author information

Reprints and permissions information is available at [www.nature.com/reprints](http://www.nature.com/reprints).

#### Competing interests

The authors declare no competing interests.

#### Corresponding author

Correspondence should be addressed to [Carola Meyer](#).

#### References

1. Upping the anti. *Nat. Phys.* **14**, 199 (2018).
2. Baltz, V. *et al.* Antiferromagnetic spintronics 2018. *Rev. Mod. Phys.* **90**, 015005 (2018).
3. Jungwirth, T., Marti, X., Wadley, P. & Wunderlich, J. Antiferromagnetic spintronics. *Nat. Nanotechnol.* **11**, 231–241 (2016).
4. Marrows, C. Addressing an antiferromagnetic memory. *Science* **351**, 558–559 (2016).
5. Atzori, M. and Sessoli, R., The second quantum revolution: role and challenges of molecular chemistry. *J. Am. Chem. Soc.* **141**, 11339–11352 (2019).
6. Gobbi, M., Novak, M. A. & Del Barco, E. Molecular spintronics. *J. Appl. Phys.* **125**, 240401 (2019).
7. Schmaus, S. *et al.* Giant magnetoresistance through a single molecule. *Nat. Nanotechnol.* **6**, 185–189 (2011).
8. Bazarnik, M. *et al.* Toward tailored all-spin molecular devices. *Nano Lett.* **16**, 577–582 (2016).
9. Karan, S. *et al.* Spin control induced by molecular charging in a transport junction. *Nano Lett.* **18**, 88–93 (2018).
11. Paschke, F., Erler, P., Enenkel, V., Gragnaniello, L. & Fonin, M. Bulk-like magnetic signature of individual Fe<sub>4</sub>H molecular magnets on graphene. *ACS Nano*, **13**, 780–785 (2019).
12. Li, J. *et al.* Electrically addressing the spin of a magnetic porphyrin through covalently connected graphene electrodes. *Nano Lett.* **19**, 3288–3294 (2019).
13. Czap, G. *et al.* Probing and imaging spin interactions with a magnetic single-molecule sensor. *Science*, **364**, 670–673 (2019).
14. Czap, G. *et al.* Detection of spin-vibration states in single magnetic molecules. *Phys. Rev. Lett.* **123**, 106803 (2019).
15. Sierda, E., Elsebach, M., Wiesendanger, R. & Bazarnik, M. Probing weakly hybridized magnetic molecules by single-atom magnetometry. *Nano Lett.* **19**, 9013–9018 (2019).
16. Yang K. *et al.* Tunable giant magnetoresistance in a single-molecule junction. *Nature Commun.* **10**, 3599 (2019).
17. Xu, Z., Liu, J., Hou, S. & Wang, Y. Manipulation of molecular spin state on surfaces studied by scanning tunneling microscopy. *Nanomat.* **10**, 2393 (2020).

18. Grose, J. E. *et al.* Tunnelling spectra of individual magnetic endofullerene molecules. *Nat. Mater.* **7**, 884–889 (2008).
19. Vincent, R., Klyatskaya, S., Ruben, M., Wernsdorfer, W. & Balestro, F. Electronic read-out of a single nuclear spin using a molecular spin transistor. *Nature* **488**, 357–360 (2012).
20. Thiele, S. *et al.* Electrically driven nuclear spin resonance in single-molecule magnets. *Science* **344**, 1135–1138 (2014).
21. Burzurí, E. *et al.* Spin-state dependent conductance switching in single molecule-graphene junctions. *Nanoscale*, **10**, 7905–7913 (2018).
22. Bogani, L. & Wernsdorfer, W. Molecular spintronics using single-molecule magnets. *Nat. Mater.* **7**, 179–186 (2008).
23. Urdampilleta, M., Klyatskaya, S., Cleuziou, J. P., Ruben, M. & Wernsdorfer, W. Supramolecular spin valves. *Nat. Mater.* **10**, 502–506 (2011).
24. Ganzhorn, M., Klyatskaya, S., Ruben, M. & Wernsdorfer, W. Strong spin-phonon coupling between a single-molecule magnet and a carbon nanotube nanoelectromechanical system. *Nat. Nanotechnol.* **8**, 165–169 (2013).
25. Urdampilleta, M., Klyatskaya, S., Ruben, M. & Wernsdorfer, W. Magnetic Interaction Between a Radical Spin and a Single-Molecule Magnet in a Molecular Spin-Valve. *ACS Nano* **9**, 4458–4464 (2015).
26. Kampert, E. *et al.* Ligand-Controlled Magnetic Interactions in Mn<sub>4</sub> Clusters. *Inorg. Chem.* **48**, 11903–11908 (2009).
27. Achilli, S. *et al.* Magnetic properties of {M<sub>4</sub>} coordination clusters with different magnetic cores (M = Co, Mn). Preprint at <https://arxiv.org/abs/2107.07237> (2021).
28. Frielinghaus, R. *et al.* Controlled covalent binding of antiferromagnetic tetramanganese complexes to carbon nanotubes. *RSC Adv.* **5**, 84119 (2015).
29. Zanolli, Z. & Charlier, J.-C., Defective carbon nanotubes for single-molecule sensing. *Phys. Rev. B* **80**, 155447 (2009).
30. Zanolli, Z. & Charlier, J.-C., Single-molecule sensing using carbon nanotubes decorated with magnetic clusters. *ACS Nano*, **6**, 10786 (2012).
31. Zanolli, Z. & Charlier, J.-C., Spin transport in carbon nanotubes with magnetic vacancy-defects, *Phys. Rev. B* **81**, 165406 (2010).
32. Schnee, M. *et al.* Quantum transport in carbon nanotubes covalently functionalised with magnetic molecules. *Phys. Status Solidi B* **253**, 2424 (2016).
33. Bockrath, M. *et al.* Single-Electron Transport in Ropes of Carbon Nanotubes. *Science* **275**, 1922–1925 (1997).
34. Piscanec, S., Lazzeri, M., Robertson, J., Ferrari, A. C. & Mauri, F. Optical phonons in carbon nanotubes: Kohn anomalies, Peierls distortions, and dynamic effects. *Phys. Rev. B* **75**, 1–22 (2007).
35. Vierck, A., Gannott, F., Schweiger, M., Zaumseil, J. & Maultzsch, J. ZA-derived phonons in the Raman spectra of single-walled carbon nanotubes. *Carbon* **117**, 360–366 (2017).
36. Sydoruk, V. A. *et al.* Low-frequency noise in individual carbon nanotube field-effect transistors with top, side and back gate configurations: effect of gamma irradiation. *Nanotechnology* **25**, 035703 (2014).
37. Ponzoni, S., Achilli, S., Pintossi, C., Drera, G., Sangaletti, L., Castrucci, P., De Crescenzi, M., Pagliara, S. Bridized C–O–Si Interface States at the Origin of

- Efficiency Improvement in CNT/Si Solar Cells, *ACS Appl. Mater. Interfaces* **19**, 16627–16634 (2017).
38. Gruneis, A., Esplandiu, M. J., Garcia-Sanchez, D. & Bachtold, A. Detecting individual electrons using a carbon nanotube field-effect Transistor. *Nano Lett.* **7**, 3766–3769 (2007).
  39. Kambly, D., Flindt, C., and Büttiker, M. Factorial cumulants reveal interactions in counting statistics. *Phys. Rev. B* **83**, 075432 (2011).
  40. Stegmann, P., Sothmann, B., Hucht, A. & König, J. Detection of interactions via generalized factorial cumulants in systems in and out of equilibrium. *Phys. Rev. B* **92**, 155413 (2015).
  41. Kurzmann, A. *et al.* Optical Detection of Single-Electron Tunneling into a Semiconductor Quantum Dot. *Phys. Rev. Lett.* **122**, 247403 (2019).
  42. Khaetskii, A. V & Nazarov, Y. V. Spin relaxation in semiconductor quantum dots. *Phys. Rev. B* **61**, 12639–12642 (2000).
  43. Martens, M., Franco, G., Dalal, N. S., Bertaina, S. & Chiorescu, I. Spin-orbit coupling fluctuations as a mechanism of spin decoherence. *Phys. Rev. B* **96**, 180408 (2017).
  44. Serri, M. *et al.* High-temperature antiferromagnetism in molecular semiconductor thin films and nanostructures. *Nat. Commun.* **5**, 1–9 (2014).
  45. Morgan, C., Misiorny, M., Metten, D., Heedt, S., Schäpers, Th., Schneider, C. M., Meyer, C. Impact of Tunnel-Barrier Strength on Magnetoresistance in Carbon Nanotubes, *Phys. Rev. Applied* **5**, 054010 (2016).
  46. Misiorny, M. and Meyer, C. Gate-voltage response of a one-dimensional ballistic spin valve without spin-orbit interaction, *Phys. Rev. Applied* **7**, 024011 (2017).
  47. García, A. *et al.*, SIESTA : Recent developments and applications, *J. Chem. Phys.* **152**, 204108 (2020)
  48. Papior, N. *et al.*, Improvements on non-equilibrium and transport Green function techniques: the next-generation TRANSIESTA, *Comput. Phys. Commun.* **212**, 8 (2017).
  49. Costa Jr., A. T., Kirwan, D. F. & Ferreira, M. S., Indirect exchange coupling between magnetic adatoms in carbon nanotubes, *Phys. Rev. B* **72**, 085402 (2005).

## Supplementary Information

### Monitoring transitions between antiferromagnetic states of individual molecules

Claire Besson, Philipp Stegmann, Michael Schnee, Zeila Zanolli, Simona Achilli, Nils Wittemeier, Asmus Vierck, Robert Frielinghaus, Paul Kögerler, Janina Maultzsch, Pablo Ordejón, Claus M. Schneider, Alfred Hucht, Jürgen König, Carola Meyer\*

\*Correspondence should be addressed to [carola.meyer@uos.de](mailto:carola.meyer@uos.de)

SI-1 Discussion of spin states in the $\{M_4\}$ complex.....	page S1
SI-2 DFT calculations of $\{Mn_4\}$ and $\{Co_4\}$ complex grafted to the carbon nanotube..	page S4
SI-3 Raman spectrum of the $\{Mn_4\}$ functionalised CNT device .....	page S12
SI-4 Histogram of the derivative of the original data .....	page S13
SI-5 Theoretical models and results.....	page S15
References .....	page S19

## SI-1 Discussion of spin states in the $\{\text{M}_4\}$ complex

In our effective spin model, we use the fact that each of the four  $\text{Mn}^{\text{II}}$  ions,  $i = 1, \dots, 4$  carries a spin  $\vec{S}_i$  with spin quantum number  $S_i = \frac{5}{2}$ , and magnetic quantum number  $S_i^z = -\frac{5}{2}, -\frac{3}{2}, \dots, \frac{5}{2}$ . This yields a  $6^4$ -dimensional Hilbert space for the spin states. Instead of characterizing the spin states by the quantum numbers  $\{S_1^z, S_2^z, S_3^z, S_4^z\}$ , we can use the standard procedure for adding angular momenta to find a basis that is more convenient for our purpose. Let  $S_{ij}$  be the spin quantum number and  $S_{ij}^z$  be the magnetic quantum number of the spin sum  $\vec{S}_{ij} := \vec{S}_i + \vec{S}_j$ . In a first step, we combine spins 1 with 2 and 3 with 4 (see Fig. S1). This leads to a new basis characterised by  $\{S_{12}, S_{12}^z, S_{34}, S_{34}^z\}$ . In a second step, we form the total spin

$$\vec{S}_{\text{tot}} := \sum_i^4 \vec{S}_i = \vec{S}_{12} + \vec{S}_{34} \quad (1)$$

with the spin quantum number  $S_{\text{tot}}$  and the magnetic quantum number  $S_{\text{tot}}^z$ . The resulting basis can be labelled by the set of quantum numbers  $\{S_{\text{tot}}, S_{\text{tot}}^z, S_{12}, S_{34}\}$ . (Alternatively, we could have chosen  $\{S_{\text{tot}}, S_{\text{tot}}^z, S_{13}, S_{24}\}$  or  $\{S_{\text{tot}}, S_{\text{tot}}^z, S_{14}, S_{23}\}$ .)

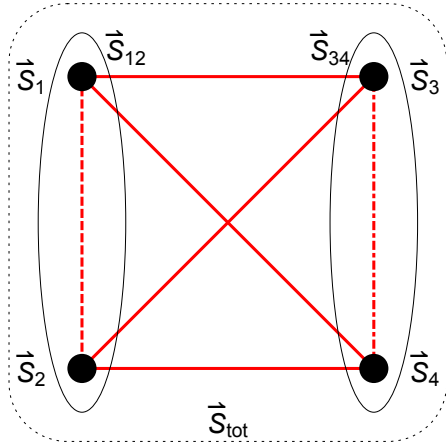


**Figure S1 | Schematic view of the spin system of the  $\{\text{Mn}_4\}$  complex.** Four  $\frac{5}{2}$ -spins are coupled to each other. If all exchange interactions are equal, the ground state is six-fold degenerate. For small deviations between the interactions, the degeneracy is split into six antiferromagnetic eigenstates of different energy.

We assume a Heisenberg-like spin-exchange coupling for each pair of Mn spins,

$$H = -\frac{1}{2} \sum_{i \neq j} J_{ij} \vec{S}_i \cdot \vec{S}_j \quad (2)$$

with antiferromagnetic  $J_{ij} < 0$ .



If all exchange couplings are equal,  $J_{ij} = J$ , we can use  $\sum_{i \neq j} \vec{S}_i \cdot \vec{S}_j = \vec{S}_{\text{tot}}^2 - \sum_i \vec{S}_i^2$ , together with  $\vec{S}_{\text{tot}}^2 = S_{\text{tot}}(S_{\text{tot}} + 1)$  and  $\vec{S}_i^2 = S_i(S_i + 1) = \frac{35}{4}$  to see that the eigenenergy

$$E = -\frac{J}{2}[S_{\text{tot}}(S_{\text{tot}} + 1) - 35] \quad (3)$$

only depends on the spin quantum number  $S_{\text{tot}}$  of the total spin but not on  $S_{\text{tot}}^Z$ ,  $S_{12}$ , or  $S_{34}$ . For antiferromagnetic coupling,  $J < 0$ , the ground state has total spin  $S_{\text{tot}} = 0$  with vanishing dipole moment,  $S_{\text{tot}}^Z = 0$ . It is six-fold degenerate with

$$|S_{\text{tot}}, S_{\text{tot}}^Z, S_{12}, S_{34}\rangle = |0, 0, 0, 0\rangle, |0, 0, 1, 1\rangle, |0, 0, 2, 2\rangle, |0, 0, 3, 3\rangle, |0, 0, 4, 4\rangle, |0, 0, 5, 5\rangle$$

Unequal  $J_{ij}$ 's remove this degeneracy. Instead of a six-fold degenerate ground state, there are now six energy eigenstates, all with  $S_{\text{tot}}, S_{\text{tot}}^Z = 0$ , as long as the variation between the different  $J_{ij}$ 's is not too large. States with  $S_{\text{tot}} > 0$  remain higher in energy. Therefore, we can conclude that both the ground and the first excited state do not carry any dipole moment, i.e.  $S_{\text{tot}}^Z = 0$ .

As an example, assuming  $J_{12} < J_{34} < J_{31} = J_{14} = J_{23} = J_{24}$  the ground state  $|\Psi_0\rangle = |0, 0, 0, 0\rangle$  and the first excited state  $|\Psi_1\rangle = |0, 0, 1, 1\rangle$  (in the  $S^Z$ -base) are given by:

Ground state:

$|\Psi_0\rangle = |\varphi_0\rangle \otimes |\varphi_0\rangle$  with

$$|\varphi_0\rangle = \frac{1}{\sqrt{6}} \left( \left| \frac{5}{2}, -\frac{5}{2} \right\rangle - \left| \frac{3}{2}, -\frac{3}{2} \right\rangle + \left| \frac{1}{2}, -\frac{1}{2} \right\rangle - \left| -\frac{1}{2}, \frac{1}{2} \right\rangle + \left| -\frac{3}{2}, \frac{3}{2} \right\rangle - \left| -\frac{5}{2}, \frac{5}{2} \right\rangle \right).$$

First excited state:

$|\Psi_1\rangle = a_{-1}|\varphi_{1,-1}\rangle \otimes |\varphi_{1,1}\rangle - a_0|\varphi_{1,0}\rangle \otimes |\varphi_{1,0}\rangle + a_1|\varphi_{1,1}\rangle \otimes |\varphi_{1,-1}\rangle$  with

$$|\varphi_{1,1}\rangle = \frac{\sqrt{10}|\frac{5}{2}, -\frac{3}{2}\rangle - 4|\frac{3}{2}, -\frac{1}{2}\rangle + 3\sqrt{2}|\frac{1}{2}, \frac{1}{2}\rangle - 4|\frac{1}{2}, \frac{3}{2}\rangle + \sqrt{10}|\frac{3}{2}, \frac{5}{2}\rangle}{\sqrt{70}},$$

$$|\varphi_{1,0}\rangle = \frac{5|\frac{5}{2}, -\frac{5}{2}\rangle - 3|\frac{3}{2}, -\frac{3}{2}\rangle + |\frac{1}{2}, -\frac{1}{2}\rangle + |\frac{1}{2}, \frac{1}{2}\rangle - 3|\frac{3}{2}, \frac{3}{2}\rangle + 5|\frac{5}{2}, \frac{5}{2}\rangle}{\sqrt{70}},$$

$$|\varphi_{1,-1}\rangle = \frac{\sqrt{10}|\frac{3}{2}, -\frac{5}{2}\rangle - 4|\frac{1}{2}, -\frac{3}{2}\rangle + 3\sqrt{2}|\frac{1}{2}, -\frac{1}{2}\rangle - 4|\frac{3}{2}, \frac{1}{2}\rangle + \sqrt{10}|\frac{5}{2}, \frac{3}{2}\rangle}{\sqrt{70}}.$$

The coefficients verify  $a_i = \frac{1}{\sqrt{3}}$  for magnetic field  $B = 0$ . They differ in case a magnetic field is applied.

The same procedure applies to  $M = \text{Co}$ , except for the difference in spin quantum number, which is only  $3/2$  for  $\text{Co}^{\text{II}}$ , so that the singlet ground state is only 4-fold (instead of 6-fold) degenerate in the case of a perfect magnetic tetrahedron. Again, the degeneracy between those states is lifted as the  $J$  couplings between centers are not identical in the actual complex.

## **SI-2 DFT calculations of $\{\text{Mn}_4\}$ and $\{\text{Co}_4\}$ complex grafted to the carbon nanotube.**

The structural, electronic and magnetic properties of the  $\{\text{M}_4\}$ -CNT hybrid systems (where  $M = \text{Mn}$  or  $\text{Co}$ ) are computed from first principles using the SIESTA<sup>1,2</sup> code. The  $\{\text{M}_4\}$

complex is bound via a  $\text{-CO}_2^-$  group to the dangling C of a mono-vacancy site on the external wall of a metallic armchair (5, 5) nanotube. The choice of a metallic nanotube ensures that electron conduction is allowed around the Fermi energy. Previous studies have demonstrated that the mono-vacancy site is especially favorable for functionalisation of CNTs with molecules<sup>3</sup> or magnetic nanoparticles.<sup>4</sup>

We consider two simulation set-ups: a supercell with periodic boundary conditions (PBC), and an open-system (OPEN) in which a single molecule is attached to an infinite tube (Fig. S2). The latter allows us to ascertain the nature of the interaction between the molecule and the CNT by avoiding spurious interaction between the periodic replica of the molecule, mediated by the electronic states of the metallic CNT.<sup>5-7</sup>

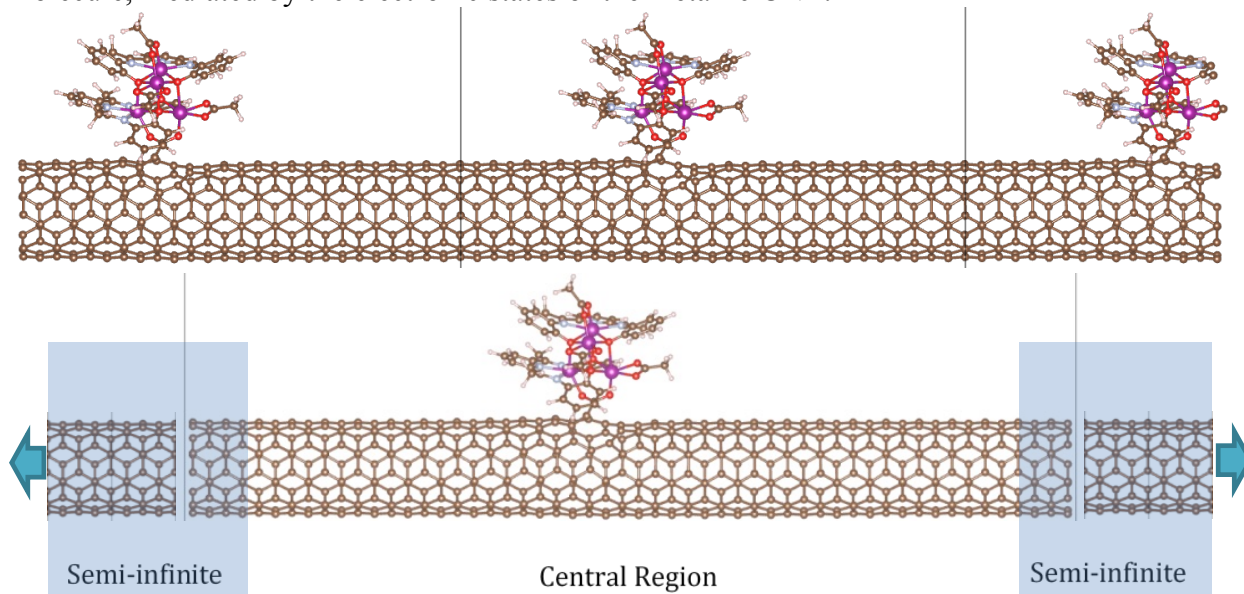


**Figure S2** | Periodic boundary conditions (top) and open system (bottom) set-up for first-principles simulations of  $\{\text{M}_4\}$ -CNT hybrid systems.

In order to take into account the strong correlation of the 3d electrons and avoid the excessive delocalisation of the  $d$  states predicted in the Local Density Approximation, Hubbard-like corrections  $U = 6$  eV and  $U = 4$  eV were used for Mn and Co, respectively (LDA+U method).<sup>8</sup> The same  $U = 6$  eV value was used by Kampert *et al.* in their calculations on  $\{\text{Mn}_4\}$ .<sup>9</sup> A standard double zeta polarised (DZP) basis set was used for carbon, nitrogen and hydrogen, and an optimised double-zeta (DZ) for Mn, Co and O. Calculations were spin polarised and performed assuming collinear spins. LDA+SOC calculations (off-site formalism of Ref. [10]) without Hubbard correction were performed in order to determine the orbital moments and the role of SOC as currently, the SIESTA code does not allow to include both SOC and Hubbard correction. We verified that the effect of spin-orbit interaction is negligible in  $\{\text{Mn}_4\}$  (as expected for a half filled  $3d$  shell) but not in  $\{\text{Co}_4\}$ . Convergence of electronic structure and magnetic properties was achieved for a real space grid cut-off of 400 Ry, and a Fermi-Dirac smearing of 100 K in the LDA+U calculation, while with SOC a cut-off of 650 Ry and electronic temperature of 1 K were adopted. The atomic positions were relaxed in standard periodic boundary conditions simulations, with a  $1 \times 1 \times 12$  k-points sampling of the Brillouin zone for 15

cells of  $\{M_4\}$ -CNT (shifted grid), and the conjugate gradient algorithm. The maximum force on atoms was smaller than 0.04 eV/Å for the CNT+ $\{M_4\}$  system.

Periodic boundary conditions simulations were performed for 15, 23, 27, and 35 armchair (5, 5) supercells to analyze the long-range decay of the induced spin polarization in the system. The supercells correspond to a distance between grafting points of 36.9, 56.6, 66.5, 86.2 Å, and a separation between the molecules of ~23.5, 43.0, 53.0, 73.0 Å, as the lateral size of the molecule is about 13.5 Å. We used a sampling of the Brillouin zone equivalent to  $1 \times 1 \times 12$  k-points for 15 cells of  $\{M_4\}$ -CNT (shifted grid). The smallest cell was adopted to find the ground state magnetic configuration of the grafted molecules (Table S1 and S2).

Open-system simulations were performed using the same computational details as for the PBC case, within a Non-Equilibrium Green's function formalism, using the TranSIESTA solution method.<sup>11-12</sup>

### **a) Periodic boundary condition simulations**

#### **a1) $\{M_4\}$ -CNT ground state magnetic configuration**

Collinear-spin PBC simulations were performed for  $\{M_4\}$ -CNT systems differing for the direction of the spin magnetic moment of the four magnetic atoms in the complex: aligned parallel (up) or antiparallel (down) to an arbitrary direction. We find that the spin configuration with lowest total energy (ground state) has total spin  $S_{\text{tot}}^z = 0$  for both isolated<sup>13</sup> and grafted molecules, and for both complexes. The ground state is labelled up-up-down-down (*uudd*) referring to the relative alignment of the four M ions. The M ions connected to the same kind of ligand are almost equivalent, as they face a similar chemical environment. In our notation, the pairs of quasi-equivalent ions are M1/M2 and M3/M4. The ground state presents an antiferromagnetic (AFM) coupling between non-equivalent M ions (M1/M3, and M2/M4), and a ferromagnetic (FM) coupling between the equivalent pairs (M1/M2 and M3/M4).

The total energy of the investigated spin configurations for the fully relaxed  $\{Mn_4\}$ -CNT and  $\{Co_4\}$ -CNT are reported in Tables S1 and S2, together with the magnetization of the four M atoms. As in the free-standing case,<sup>13</sup> the absolute values of the magnetic moments of the two not equivalent pairs of magnetic atoms are slightly different. However, the molecules maintain a total spin  $S_{\text{tot}}^z \sim 0$  in the AFM configurations, due to the spin polarization of the ligands, which is more relevant in  $\{Co_4\}$ .

Config.	$\Delta E$ [meV]	$\mu^S_1 [\mu_B]$	$\mu^S_2 [\mu_B]$	$\mu^S_3 [\mu_B]$	$\mu^S_4 [\mu_B]$
<b>uudd</b>	<b>0.0</b>	<b>4.82</b>	<b>4.82</b>	<b>-4.88</b>	<b>-4.87</b>
uddu	2.2	4.82	-4.82	-4.88	4.87
uduu	3.7	4.82	-4.82	4.88	4.87
uuud	5.1	4.82	4.82	4.88	-4.87
uddd	5.5	4.82	-4.82	-4.88	-4.87
uuuu	8.0	4.83	4.82	4.88	4.87
udud	12.8	4.82	-4.82	4.88	-4.87

**Table S1** | Low-energy magnetic configurations for the  $\{Mn_4\}$ -CNT obtained from periodic boundary conditions DFT+U calculations. The ground state (uudd) is highlighted in bold. We report the total energy with respect to the ground state configuration ( $\Delta E$ , in

meV), and the spin magnetic moment for each ion. The units of the magnetic moment are Bohr magnetons ( $\mu_B$ ). The data refer to the 15 cells PBC calculation.

Config.	$\Delta E$ [meV]	$\mu^S_1 [\mu_B]$	$\mu^S_2 [\mu_B]$	$\mu^S_3 [\mu_B]$	$\mu^S_4 [\mu_B]$
<b>uudd</b>	<b>0.0</b>	<b>2.70</b>	<b>2.71</b>	<b>-2.72</b>	<b>-2.73</b>
dddu	10.0	-2.71	-2.71	2.72	-2.74
udud	10.3	-2.70	2.71	-2.72	2.74
uudu	10.9	2.70	2.71	2.72	-2.73
uddd	14.9	-2.71	2.71	-2.72	-2.74
uuuu	18.1	2.71	2.71	2.73	2.74
uddu	20.3	-2.65	2.79	2.65	-2.79

**Table S2** | Low-energy magnetic configurations for the  $\{\text{Co}_4\}$ -CNT obtained from periodic boundary conditions DFT+U calculations. The ground state (uudd) is highlighted in bold. We report the total energy with respect to the ground state configuration ( $\Delta E$ , in meV), and the spin magnetic moment for each magnetic ion. The units of the magnetic moment are Bohr magnetons ( $\mu_B$ ). The data refer to the 15 cells PBC calculation.

### a2) $\{M_4\}$ - CNT electronic band structure

All the hybrid  $\{M_4\}$ -CNT-systems we modelled are metallic, as illustrated by their electronic band structure (Fig. S3). The  $\{M_4\}$  complex does not perturb much the electronic structure of the nanotube in the vicinity of the Fermi energy, indicating that the interaction between nanotube and molecule is weak and explaining why the magnetic properties of the  $\{M_4\}$  complex are preserved after bonding to the nanotube. The weak interaction between tube and molecule only causes minor changes in the band structure of the other explored magnetic configurations (not shown). The band structure of the two systems looks very similar, featuring the dispersing bands of CNT (5,5) that are slightly spin polarised and dispersionless (flat) bands whose spin polarisation is larger. These bands that lie above the Fermi level (at  $\sim 0.5$  eV for  $\{Mn_4\}$  and  $\sim 0.3$  eV for  $\{Co_4\}$  in the LDA+U calculation – on the left) correspond to energy levels localised on the  $\{M_4\}$  complex. In the calculation with SOC (right) the bands show the same properties apart for a shift of the dispersionless bands toward the Fermi level (for both occupied and empty states) due to the absence of the Hubbard U correction that accounts for the electronic correlation.

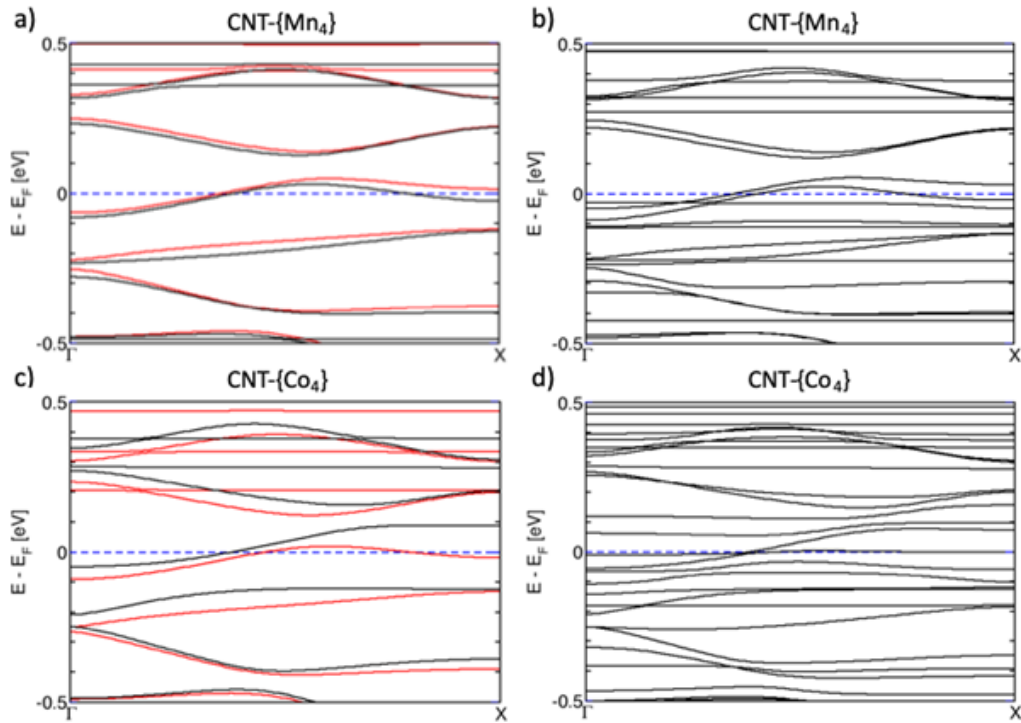


**Figure S3** | Electronic band structure of a CNT functionalised with a  $\{Mn_4\}$  or  $\{Co_4\}$  complex computed in the LDA+U approximation (red: majority spins, black: minority spins, panels a and c), or explicitly including SOC (panel b and d). Flat bands in the electronic structure correspond to the energy levels of the complex. The Fermi level is indicated with a dashed blue line.

## 2) Open system simulations

### 2a) LDA+U: charge transfer between molecule and tube and localized magnetic moments

Charge transfer was computed in the open system set up. Regardless of the spin configuration, the  $\{\text{Mn}_4\}$  complex always *withdraws* electron charge from the CNT. In the ground state *uudd* configuration the dangling C in the CNT donates 0.08 electrons while the electronic charge transferred from the other eight C atoms near the  $-\text{CO}_2^-$  group (highlighted in yellow in Fig. S4) is 0.1 electrons, for a total of 0.18 electrons donated by the atoms surrounding the monovacancy.

The charge transfer is different for majority and minority spin electronic charge leading to a small magnetic moment of the molecule ( $\mu_{\{\text{Mn}_4\}} = -0.006 \mu_B$ ) in the ground state configuration, differently from the free-standing case where it was exactly zero. An induced spin polarization is found on the CNT giving  $\mu_{\{\text{CNT}\}} = -0.025 \mu_B$  in the cell. The associated spin density is delocalised over the whole CNT as shown in Fig. 1 of the main manuscript. The C acting as linking site retains a magnetic moment of  $-0.021 \mu_B$  while the other eight C atoms belonging to the defect site have a total magnetic moment of  $-0.004 \mu_B$ . Even though the induced spin polarisation is most important at the functionalized vacancy site, the effect is long ranged and allows for a correlation among the spin state of various molecules grafted to the tube.

In  $\{\text{Co}_4\}$ -CNT ground state the charge transfer from the linking C to the molecule amounts to 0.13 electrons, larger than in  $\{\text{Mn}_4\}$ -CNT while for the other eight C atoms near the  $-\text{CO}_2^-$  group it is 0.03 electrons, i.e. smaller than in the other system.

The linking C has an induced magnetic moment of  $0.084 \mu_B$  in  $\{\text{Co}_4\}$ -CNT which is larger, in modulus, than the value found in  $\{\text{Mn}_4\}$ -CNT. On the other hand, the sum of the magnetic moments of the other eight atoms forming the defect in the CNT is  $0.006 \mu_B$  in  $\{\text{Co}_4\}$ -CNT. The magnetic moment on the molecule is  $0.021 \mu_B$  while the net spin polarization induced on the portion of the CNT in the unit cell is  $0.117 \mu_B$  i.e. larger than the other compound ( $\mu_{\{\text{CNT}\}} = -0.03 \mu_B$ ).

The percentage of the magnetic moment of the C atoms of the CNT in the cell which is localized on the C atoms of the defect at the linking site (linking C + 8 C atoms) is 76% for  $\{\text{Co}_4\}$ -CNT and 95% for  $\{\text{Mn}_4\}$ -CNT.

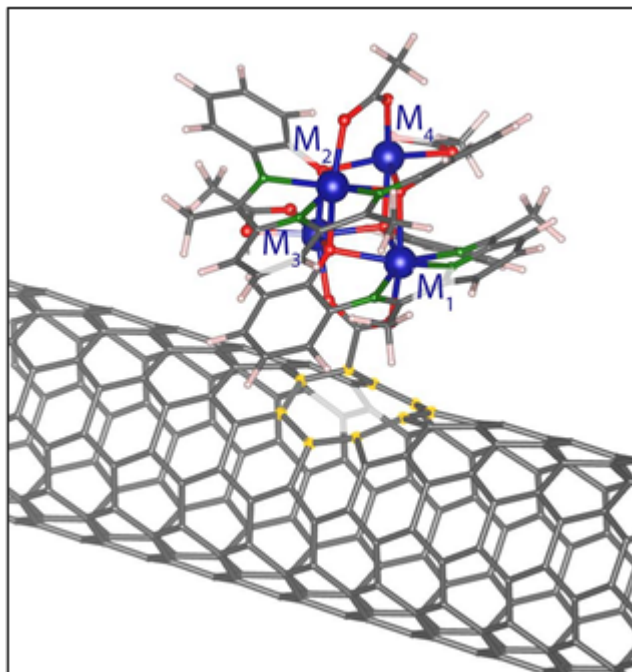


**Figure S4** | Linking of the molecule to the CNT. Color code: C - grey, O - red, N - green, Mn/Co - blue. The atoms surrounding the mono-vacancy site where the molecule is grafted to the tube are highlighted in yellow.

## 2b) LDA+U: Magnetic moment on the CNT- $\{M_4\}$ hybrid systems

We compare the magnetic moments obtained in the open system setup with the values calculated for the periodic system by increasing the PBC cell size. We verified that the magnetic moment of  $\{Mn_4\}$ -CNT tends to the open system solution ( $0.03 \mu_B$ ) while this is not the case for  $\{Co_4\}$ -CNT, where the PBC magnetic moment is not converged even in the 35-cells case (Table S3). This is due to the long-range character of the indirect exchange coupling between magnetic cluster mediated by the conduction electrons of metallic carbon nanotubes<sup>5</sup>. Therefore, we base our analysis of the spin and orbital moment in the OPEN system setup. From the latter, we find that the magnetic moment of the  $\{Co_4\}$ -CNT system is  $0.14 \mu_B$ , an order of magnitude larger than in the  $\{Mn_4\}$ -CNT case. The spin moment induced in the tube is larger for the  $\{Co_4\}$  case, indicating that the nature of the interaction between  $\{Co_4\}$  molecules is longer range than  $\{Mn_4\}$ , and reflected in the interaction between the periodic replica. On the other hand, the decay of the magnetic perturbation in the two system is similar (figure S5), as it is determined by the conduction electrons of the nanotube.

Molecule (#CNT-Rings)	S  PBC [ $\mu_B$ ]	S  Open System [ $\mu_B$ ]
Mn <sub>4</sub> (15)	0.23	
Mn <sub>4</sub> (23)	0.17	0.03

Mn <sub>4</sub> (27)	0.08	0.03
Mn <sub>4</sub> (35)	0.06	0.03
Co <sub>4</sub> (15)	0.18	
Co <sub>4</sub> (23)	0.26	0.15
Co <sub>4</sub> (27)	0.45	0.15
Co <sub>4</sub> (35)	0.33	0.14

**Table S3** | Magnetic moments of {Mn<sub>4</sub>}-CNT and {Co<sub>4</sub>}-CNT computed in the LDA+U approximation setup for different cell size with periodic boundary condition (PBC) and for the open system. For the open system calculation, the number of CNT-rings given in parenthesis corresponds to the extension of the scattering region between semi-infinite electrodes. The units of the magnetic moment are Bohr magnetons ( $\mu_B$ ).

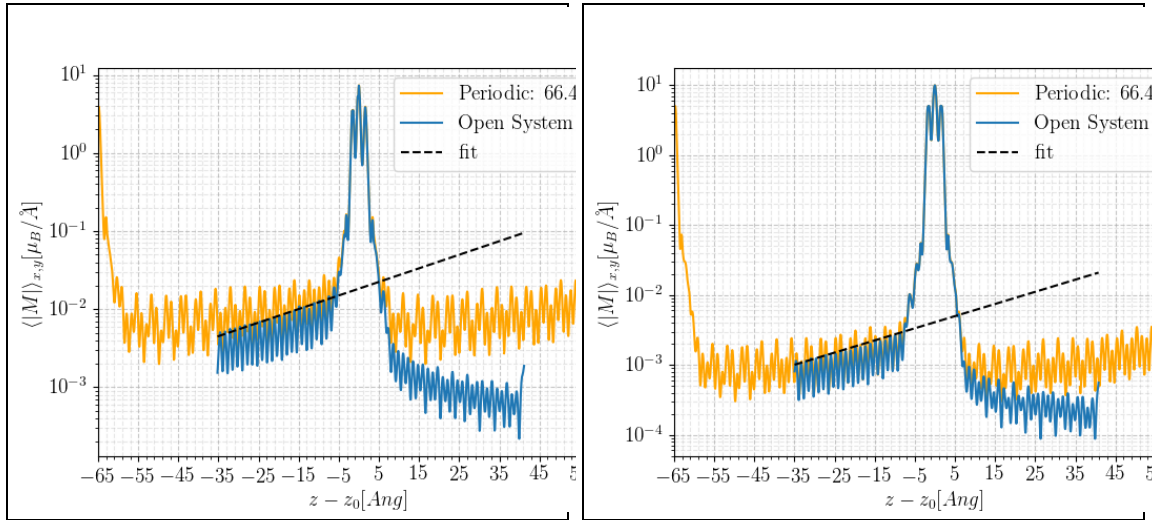


**Figure S5** | (Open System) Absolute value of spin density integrated over  $x$  and  $y$  ( $z = 0$  located at the molecule) for the {Co<sub>4</sub>}-CNT (left) and {Mn<sub>4</sub>}-CNT (right). The decay of the spin density in the open system is exponential: {Co<sub>4</sub>}-CNT:  $\exp(0.04 \cdot Z - 4)$  {Mn<sub>4</sub>}-CNT:  $\exp(0.04 \cdot Z - 5.5)$ . The asymmetry in the blue curve is due to the asymmetry of the molecule-CNT link. This effect is not visible in PBC due to the periodic repetition of the grafted molecules.

## 2b) SOC: Orbital moment on the CNT-{M<sub>4</sub>} hybrid systems

The magnetic moments and orbital angular moments on the individual magnetic sites computed for the open system with SOC and without Hubbard correction are given Table S4. The data refer to the ground-state (uudd) configuration. We note a slight reduction of the magnetic moments compared to the calculation with Hubbard correction and without SOC (Table S5): approximately  $0.25 \mu_B$  for {Co<sub>4</sub>}-CNT and  $0.15 \mu_B$  for {Mn<sub>4</sub>}-CNT. The orbital angular moments are finite in {Co<sub>4</sub>} due to the 3d<sup>7</sup> atomic configuration and are almost negligible in {Mn<sub>4</sub>} due to the half filling of the 3d shell.

SOC	$\mu^{S_1} [\mu_B]$	$\mu^{S_2} [\mu_B]$	$\mu^{S_3} [\mu_B]$	$\mu^{S_4} [\mu_B]$	$\mu^{L_1} [\mu_B]$	$\mu^{L_2} [\mu_B]$	$\mu^{L_3} [\mu_B]$	$\mu^{L_4} [\mu_B]$
{Mn <sub>4</sub> }	4.55	4.55	-4.65	-4.61	0.06	0.06	0.07	0.07
{Co <sub>4</sub> }	2.56	2.54	-2.60	-2.55	0.16	0.14	0.18	0.25



**Table S4** | Magnetic moments and orbital angular moments on the individual magnetic sites of {Mn<sub>4</sub>}-CNT and {Co<sub>4</sub>}-CNT computed from first-principles in the open-system set-up.

LDA+U	$\mu^{S_1} [\mu_B]$	$\mu^{S_2} [\mu_B]$	$\mu^{S_3} [\mu_B]$	$\mu^{S_4} [\mu_B]$	$\mu^S_{\text{Molecule}}$
{Mn <sub>4</sub> }	4.82	4.82	-4.88	-4.87	-0.031
{Co <sub>4</sub> }	2.71	2.70	-2.73	-2.72	0.138

**Table S5** | Magnetic moments on the individual magnetic sites in {Mn<sub>4</sub>}-CNT and {Co<sub>4</sub>}-CNT and residual magnetic moment of the whole {Mn<sub>4</sub>} and {Co<sub>4</sub>} molecules computed from first-principles in the open-system set-up with LDA+U.

### SI-3 Raman spectrum of the {Mn<sub>4</sub>} functionalised CNT device

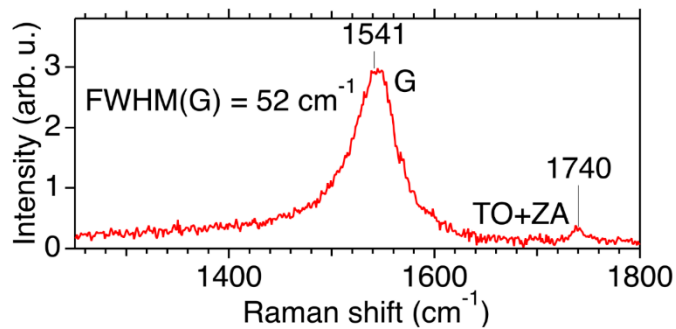


**Figure S6 | Raman spectrum of the {Mn<sub>4</sub>} functionalised CNT device.** Shape and position of the G<sup>(-)</sup>-mode and the TO+ZA combination mode in combination with the absence of the TO peak suggest a (15,0) zigzag-CNT.<sup>14</sup>

#### SI-4 Histogram of the derivative of the original data

Since the influence of the slow fluctuations (time scale 10 seconds) on the derivative with (almost) equidistant points with  $\Delta t \approx 100$  ms is negligibly small, we use the derivative of the original data to determine the expected standard deviation of the original data  $\sigma$  which is directly related to the standard deviation of the derivative  $\sigma_{\text{deriv}}$  with  $\sigma_{\text{deriv}} = \sigma \sqrt{2}$ .

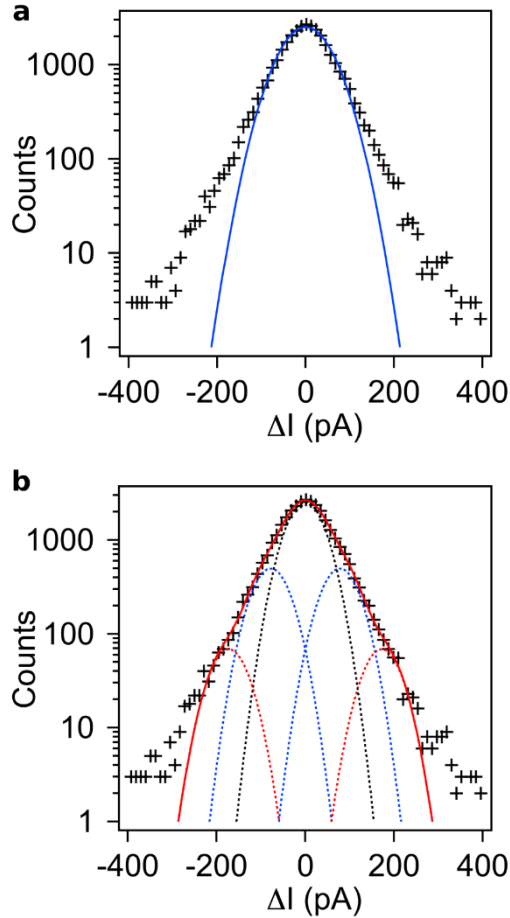


**Figure S7** | Histogram of the derivative of the current time traces (black crosses). **a** Fit with a single gaussian peak (blue solid line) **b** Fit with five gaussian peaks symmetric around 0 (red solid line) revealing the transitions for one current level (blue dotted line) and two current levels (red dotted lines).

Figure S7 compares the fit of the histogram with a single gauss peak with the fit of the histogram with five gauss peaks. It is obvious that the data (black crosses) cannot be described with a single gauss peak fit (Fig. S7a, blue solid line). Additional peaks are necessarily symmetric around zero, since the system is clearly neither continuously excited nor relaxed below a ground level. We assume the same standard deviation for all current levels and thus all transitions between levels. Assuming five gauss peaks with the second pair of gauss peaks (Fig S7b, red dotted lines) have twice the  $\Delta I$  of the first pair (Fig S7b, blue dotted lines) yields the best fit. The latter constrain does not change the residuum compared to a free position as additional fit parameter. We thus end up with a set of five fit parameters for the five curves: The width, the position of the first pair of gauss peaks,

the amplitude of the central peak, and the two amplitudes of the two pairs of gauss peaks respectively.

We find a standard deviation of  $\sigma_{\text{deriv}} = 56.4 (1.3)$  pA and thus derive a standard deviation of  $\sigma = 40 (1)$  pA for the level broadening in the original data after background correction.

## SI-5 Theoretical models and results

We model the RTS of the  $\{\text{Co}_4\}$ - and  $\{\text{Mn}_4\}$ -functionalised CNT quantum dot by a master equation visualised in figure S8a and b, respectively. The current levels (three in Fig. 2e and 14 in Fig. 2a in the main paper) correspond to energies with equidistant spacing  $\Delta\varepsilon$ . We assume that each complex can be excited just once by this amount of energy. For level 0, all  $K$  complexes are in their ground state. Each excitation of the molecules attached to the CNT leads to an increase of the level number by one. The main difference between the  $\{\text{Co}_4\}$  and the  $\{\text{Mn}_4\}$  systems is how the excitation by energy  $\Delta\varepsilon$  is distributed among the grafted complexes. This strongly affects the different transition rates between the levels and, thus, the RTS.

For the  $\{\text{Co}_4\}$ -system, each excitation is localised at one complex only, i.e. the complexes are excited independently of each other. For  $K = 70$   $\{\text{Co}_4\}$  complexes there are  $K = 70$  possibilities to choose the first complex to be excited (transition from level 0 to level 1) and  $K - 1 = 69$  possibilities to choose the second (transition from level 1 to level 2).

For the relaxation from level 1 to level 0, there is no choice but one has to pick the given excited molecule, while for relaxation from level 2 to level 1 two excited molecules are available. In addition to these combinatory factors, there is a Boltzmann factor  $r = e^{-\beta\Delta\varepsilon}$  for the excitation relative to the relaxation. The rate  $\Gamma$  sets the overall time scale. This leads to the transition rates depicted in Fig. S8a.

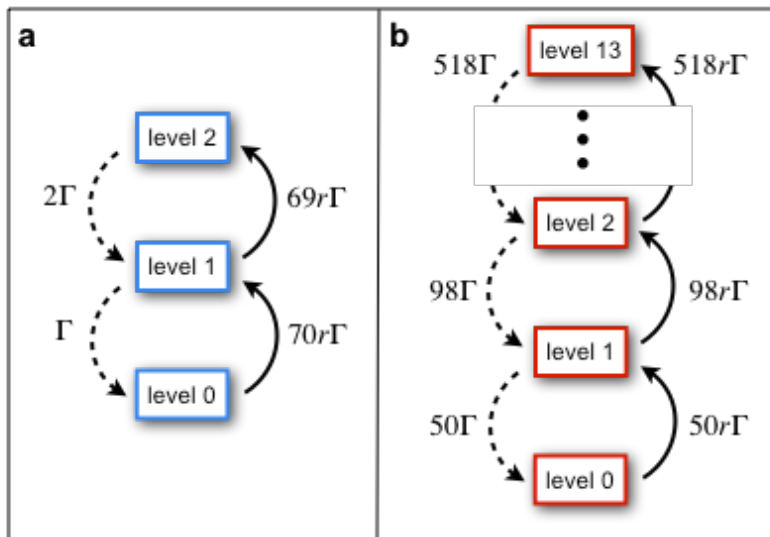


**Figure S8 | Sketch of the current levels and the transition rates.** a, the  $\{\text{Co}_4\}$ - and b, the  $\{\text{Mn}_4\}$ -functionalised CNT-quantum-dot device with transitions rate  $\Gamma$  and a Boltzmann factor  $r$ . Dashed lines indicate the counted transitions.

For the  $\{\text{Mn}_4\}$ -system, we assume *collective* excitations involving *all*  $K = 50$   $\{\text{Mn}_4\}$  complexes. The excited states of the full system are coherent superpositions of the excitations of individual complexes. Beginning from the lowest level  $|\psi_0\rangle = |0,0,0, \dots, 0\rangle$  with each complex in its ground state 0, we construct the states for the higher levels by applying the bosonic operator  $\sum_{k=1}^K a_k^\dagger$ , where  $a_k^\dagger$  excites complex  $k$  (but only if it is in its ground state), and by normalizing the state afterwards. We obtain

$$|\psi_n\rangle = \frac{1}{\sqrt{\binom{K}{n}}} \left( \sum_{k=1}^K a_k^\dagger \right)^n |0,0,0, \dots, 0\rangle, \quad (1)$$

which leads to the matrix elements

$$|\langle \psi_{n+1} | \sum_{k=1}^K a_k^\dagger | \psi_n \rangle|^2 = (K - n)(n + 1)$$

and, thus, to the rates depicted in Fig. S8b.

To calculate the factorial cumulants

$$C_{F,m}(\Delta t) = \langle \langle N(N-1) \dots (N-m+1) \rangle \rangle = \partial_z^m \ln M_F(z, \Delta t)|_{z=0}$$

for the  $\{\text{Co}_4\}$ -functionalised CNT quantum dot (and similar for  $\{\text{Mn}_4\}$ ) assuming  $K$   $\{\text{Co}_4\}$  complexes, we write the master equation in the  $N$ -resolved form

$$\dot{P}_{N,0}(\Delta t) = -Kr\Gamma P_{N,0}(\Delta t) + P_{N-1,0}(\Delta t), \quad (2)$$

$$\dot{P}_{N,1}(\Delta t) = Kr\Gamma P_{N,0}(\Delta t) - (1 + (K-1)r)\Gamma P_{N,1}(\Delta t) + 2\Gamma P_{N-1,2}(\Delta t), \quad (3)$$

$$\dot{P}_{N,2}(\Delta t) = (K-1)r\Gamma P_{N,1}(\Delta t) - 2\Gamma P_{N,2}(\Delta t). \quad (4)$$

Here  $P_{N,n}(\Delta t)$  is the probability that  $N$  transitions have occurred and the system is in level  $n$  at the end of the time interval  $\Delta t$ . After a  $z$ -transform,<sup>15,16</sup> we obtain the generating function  $M_F(z, \Delta t) = \vec{e}^T \exp[\mathbf{W}_{z+1} \Delta t] \vec{P}_{\text{stat}}$  with  $\vec{e}^T = (1, 1, 1)$  and the stationary density matrix given by  $\mathbf{W}_1 \vec{P}_{\text{stat}} = (0, 0, 0)^T$  and  $\vec{e}^T \vec{P}_{\text{stat}} = 1$ . The matrix  $\mathbf{W}_z$  is given by

$$\mathbf{W}_z = \begin{pmatrix} -Kr & z & 0 \\ Kr & -1 - (K-1)r & 2z \\ 0 & (K-1)r & -2 \end{pmatrix} \Gamma. \quad (5)$$

For the simulations presented in Fig. 3 of the main paper, the two parameters  $\Gamma$  and  $r$  have been determined such that the simulation reproduces the first factorial cumulant  $C_{F,1}(10\text{s})$  and the ratio  $P_{\text{occ}}(\psi_1)/P_{\text{occ}}(\psi_0)$  of the occupations of level 1 and 0 exactly. Higher-order factorial cumulants and the probability of the higher levels are then a result of the simulation without any further fitting parameter.

In case of a system in which the counted transitions happen independently from each other, the sign of the  $m$ -th factorial cumulant must be  $(-1)^{m-1}$  for all  $\Delta t$ .<sup>16-18</sup> This is, indeed, the case for independent two-level fluctuators, in accordance with the  $\{\text{Co}_4\}$ -data (blue curves in Fig. 3c-e of the main paper). The  $\{\text{Mn}_4\}$ -data (red curves in Fig. 3c-e of the main paper) show a different behaviour, i.e. they cannot be modelled by independent two-level fluctuators. The assumption of coherent superpositions of the excitations, on the other hand, can reproduce the data.

For completeness, we check yet another model for the  $\{\text{Mn}_4\}$ -data. Let us assume local excitations of independent *three-level* fluctuators, i.e. each complex can accommodate *two* excitations which, by chance, happen to have the same excitation energy. In Fig. S9, we depicted the results for this model (Fig. S9a). The additional parameter  $\tilde{\Gamma}$  is determined such that the simulation reproduces  $C_{F,2}(10\text{s})$  exactly. Indeed, the cumulants observed in the experiment can be reproduced by the simulation (Fig. S9c, d, and e). However, the occupation probabilities  $\mathcal{P}_{\text{occ}}$  are not recovered (Fig. S9b). Similar as for the two-level fluctuators, the combinatorial factors associated with the degeneracy of the levels strongly suppress the occupation probabilities in comparison to ones extracted from the measurements. Furthermore, very different values of  $\tilde{\Gamma}$  and  $\Gamma$  would be needed without any physical justification. We, thus, conclude that only the model assuming coherent superpositions can reproduce the measured data.

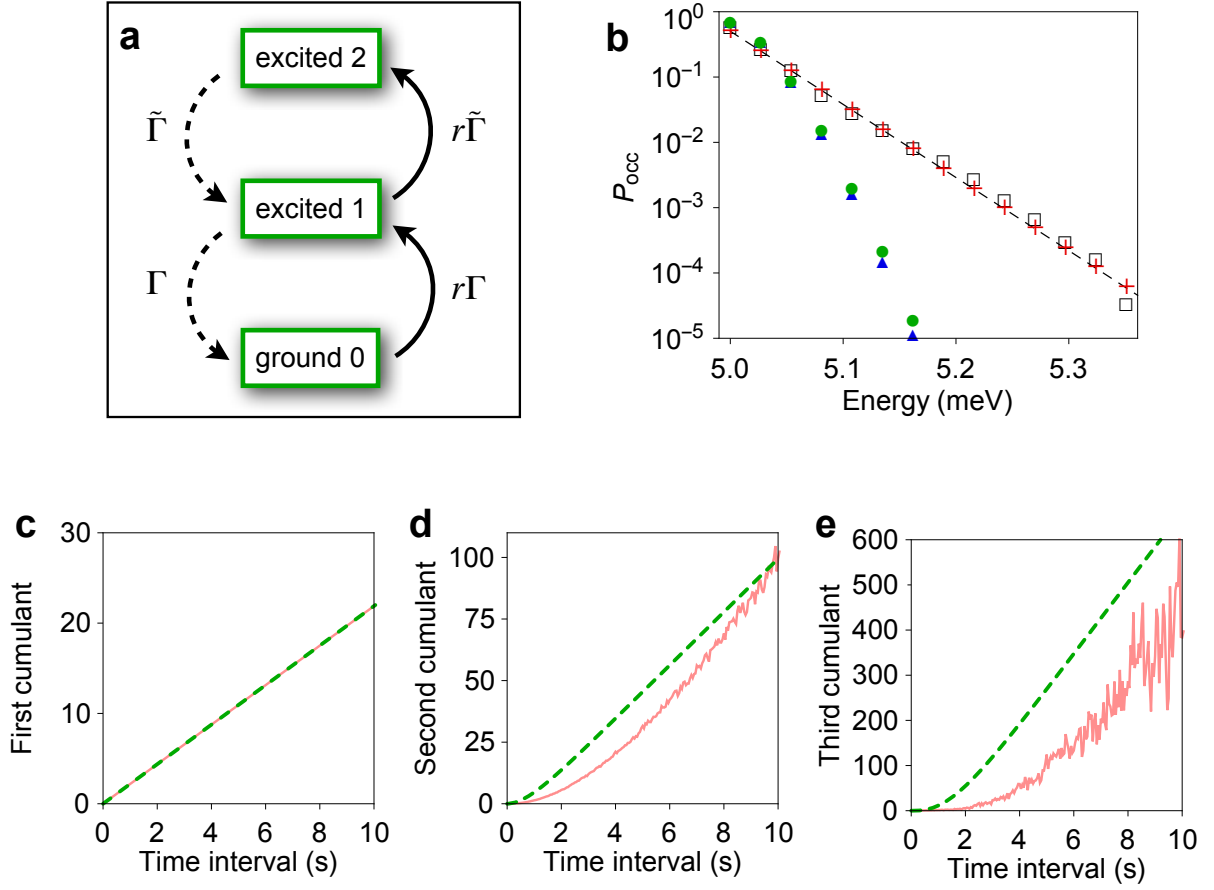


**Figure S9 | Sketch and modelling of a three-level fluctuator.** **a**, States and possible transitions of a three-level fluctuator. **b**, Occupation probability on a logarithmic scale for the different levels for the original data (black squares), and for models assuming  $K = 50$  independent two-level fluctuators (blue triangles),  $K = 50$  independent three-level fluctuators (green dots), and  $K = 50$  coherently coupled two level fluctuators (red crosses). **c**, **d**, **e**, First, second, and third factorial cumulant as extracted from the measurements (red solid line) and a simulation assuming  $K = 50$  independent three-level fluctuators (green dashed line) with  $r = 0.01$ ,  $\Gamma = 1.25/s$ , and  $\tilde{\Gamma} = 316.99/s$ .



## References

1. Soler, J. M., Artacho, E., Gale, J. D., Garcí, A., Junquera, J., Ordejon, P. and Sanchez-Portal D. The SIESTA method for ab initio order-N materials simulation. *J. Phys.: Condens. Matter* **14**, 2745 (2002).
2. García, A., Papior, N., Akhtar, A., Artacho, E., Blum, V., Bosoni, E., Brandimarte, P., Brandbyge, M., Cerdá, J. I., Corsetti, F., Cuadrado, R., Dikan, V., Ferrer, J., Gale, J., García-Fernández, P., García-Suárez, V. M., García, S., Huhs, G., Illera, S., Korytár, R., Koval, P., Lebedeva, I., Lin, L., López-Tarifa, P., Mayo, S. G., Mohr, S., Ordejón, P., Postnikov, A., Pouillon, Y., Pruneda, M., Robles, R., Sánchez-Portal, D., Soler, J. M., Ullah, R., Yu, V. W. and Junquera, J. Siesta: Recent developments and applications. *J. Chem. Phys.* **152**, 204108 (2020).
3. Zanolli, Z. and Charlier, J.-C. Defective carbon nanotubes for single-molecule sensing. *Phys. Rev. B* **80**, 155447 (2009).
4. Zanolli, Z. and Charlier, J.-C. Single-molecule sensing using carbon nanotubes decorated with magnetic clusters. *ACS Nano* **6**, 10786 (2012).
5. Costa, Jr., A. T., Kirwan, D. F. and Ferreira, M. S. Indirect exchange coupling between magnetic adatoms in carbon nanotubes. *Phys. Rev. B*, **72**, 085402 (2005).
6. Kirwan, D. F., Rocha, C. G., Costa, A. T. and Ferreira, M. S. Sudden Decay of Indirect Exchange Coupling between Magnetic Atoms on Carbon Nanotubes. *Phys. Rev. B* **77**, 085432 (2008).
7. Zanolli, Z. and Charlier, J.-C. Spin transport in carbon nanotubes with magnetic vacancy-defects. *Phys. Rev. B* **81**, 165406 (2010).
8. Dudarev, S. L., Botton, G. A., Savrasov, S. Y., Humphreys, C. J. and Sutton A. P. Electron-energy-loss spectra and the structural stability of nickel oxide: An LSDA+U Study, *Phys. Rev. B* **57**, 1505 (1998).
9. Kampert, E., Janssen, F. F. B. J., Boukhvalov, D. W., Russcher, J. C., Smits, J. M. M., de Gelder, R., de Bruin, B., Christianen, P. C. M., Zeitler, U., Katsnelson, M. I., Maan, J. C., and Rowan, A. E. Ligand-Controlled Magnetic Interactions in Mn<sub>4</sub> Clusters. *Inorg. Chem.* **48**, 11903-11908 (2009).
10. Cuadrado, R. & Cerdá, J. I. Fully relativistic pseudopotential formalism under an atomic orbital basis: spin-orbit splittings and magnetic anisotropies, *J. Phys.: Condens. Matter* **24**, 086005 (2012).
11. Brandbyge, M., Mozos, J.-L., Ordejón, P., Taylor, J. and Stokbro, K. Density-functional method for nonequilibrium electron transport, *Phys. Rev. B* **65**, 165401 (2002).
12. Papior, N., Lorente, N., Frederiksen, T., García, A., Brandbyge, M. Improvements on non-equilibrium and transport Green function techniques: The next-generation TRANSIESTA. *Comp. Phys. Commun.* **212**, 8–24 (2017).
13. Achilli, S. *et al.* Magnetic properties of {M<sub>4</sub>} coordination clusters with different magnetic cores (M = Co, Mn). Preprint at <https://arxiv.org/abs/2107.07237> (2021).
14. Reich, S., Thomsen, C., Maultzsch, J. *Carbon Nanotubes* (Wiley-VCH Berlin, 2004).

15. Johnson, N. L., Kemp, A. W. and Kotz, S. *Univariate Discrete Distributions* (John Wiley & Sons, Inc., Hoboken, 2005).
16. Stegmann, P., Sothmann, B., Hucht, A. and König, J. Detection of interactions via generalized factorial cumulants in systems in and out of equilibrium. *Phys. Rev. B* **92**, 155413 (2015).
17. Kambly, D., Flindt, C. and Büttiker, M. Factorial cumulants reveal interactions in counting statistics. *Phys. Rev. B* **83**, 075432 (2011).
18. Stegmann, P. and König, J. Short-time counting statistics of charge transfer in Coulomb-blockade systems. *Phys. Rev. B* **94**, 125433 (2016).